Remote Sensing of Tropospheric Aerosols from Space: Past, Present, and Future

Michael D. King,* Yoram J. Kaufman,* Didier Tanré,+ and Teruyuki Nakajima#

ABSTRACT

Tropospheric aerosol particles originate from man-made sources such as urban/industrial activities, biomass burning associated with land use processes, wind-blown dust, and natural sources. Their interaction with sunlight and their effect on cloud microphysics form a major uncertainty in predicting climate change. Furthermore, the lifetime of only a few days causes high spatial variability in aerosol optical and radiative properties that requires global observations from space.

Remote sensing of tropospheric aerosol properties from space is reviewed both for present and planned national and international satellite sensors. Techniques that are being used to enhance our ability to characterize the global distribution of aerosol properties include well-calibrated multispectral radiometers, multispectral polarimeters, and multiangle spectroradiometers. Though most of these sensor systems rely primarily on visible to near-infrared spectral channels, the availability of thermal channels to aid in cloud screening is an important additional piece of information that is not always incorporated into the sensor design. In this paper, the various satellite sensor systems being developed by Europe, Japan, and the United States are described, and the advantages and disadvantages of each of these systems for aerosol applications are highlighted. An important underlying theme is that the remote sensing of aerosol properties, especially aerosol size distribution and single scattering albedo, is exceedingly difficult. As a consequence, no one sensor system is capable of providing totally unambiguous information, and hence a careful intercomparison of derived products from different sensors, together with a comprehensive network of ground-based sunphotometer and sky radiometer systems, is required to advance our quantitative understanding of global aerosol characteristics.

1. Introduction

Tropospheric aerosols are important components of the earth–atmosphere–ocean system, affecting climate through three primary mechanisms. First, direct radiative forcing results when radiation is scattered or absorbed by the aerosol itself. Scattering of shortwave radiation enhances the radiation reflected back to space, therefore increasing the reflectance (albedo) of the earth and cooling the climate system. Absorption of solar and longwave radiation alters the atmospheric heating rate, which in turn may result in changes to the atmospheric circulation. Second, indirect radiative forcing results when enhanced concentrations of aerosol particles modify cloud properties, resulting in more cloud drops, albeit smaller in size, that generally increase the albedo of clouds in the earth's atmosphere. Additional cloud properties beyond cloud droplet concentration and particle size, such as enhanced liquid water content and increased cloud lifetime, have also been observed under certain circumstances. Finally, aerosol particles can have an indirect effect on heterogeneous chemistry, which in turn can influence climate by modifying the concentration of climate-influencing constituents (such as greenhouse gases). These three mechanisms are discussed in further detail by Schwartz et al. (1995).

Aerosol forcing of climate reemerged in the last few decades of the twentieth century as a key climate change component causing significant uncertainty in the radiative forcing of climate (Twomey et al. 1984;

*NASA/Goddard Space Flight Center, Greenbelt, Maryland.
+Centre National de la Recherche Scientifique, Université des Sciences des Techniques de Lille, Villeneuve d'Ascq, France.
#Center for Climate System Research, University of Tokyo, Tokyo, Japan.
Corresponding author address: Dr. Michael D. King, Earth Sciences Directorate, NASA/Goddard Space Flight Center, Code 900, Greenbelt, MD 20771.
E-mail: king@climate.gsfc.nasa.gov
In final form 11 June 1999.
©1999 American Meteorological Society

Charlson et al. 1992). In comparison to the radiative forcing of greenhouse gases of 2.5 ±0.3 W m^{-2}, the aerosol forcing through direct interaction with sunlight and indirectly through cloud modification is –1.4 ±1.5 W m^{-2} for sulfates (Houghton et al. 1996), and perhaps as large as –2.5 ±2 W m^{-2} once organic aerosols are introduced. This effect and its uncertainty are large and have to be resolved before climate models can be used reliably to predict climate change. It is exceedingly difficult to link changes in the earth's radiation budget of 1 W m^{-2}, or changes in cloud reflectance of 0.01, to changes in aerosol concentration. It is even more difficult to estimate the changes in climate that occurred in the last century due to aerosol particles, since accurate measurements have only begun to emerge in the last couple of decades. Since the aerosol lifetime is at most a few days, heterogeneous patterns of radiative forcing are generated, with large variations in optical thickness and radiative forcing of the order of tens of Watts per square meter on a regional scale [e.g., Tegen et al. (1996) for dust; Christopher et al. (1996) for smoke]. These variations give rise to the 1–2 W m^{-2} forcing on a global scale. Preliminary estimates based on aerosol simulations show that for biomass burning aerosol about 70% of the aerosol direct radiative forcing comes from regions with enhanced optical thickness in excess of 0.1 (Remer et al. 1999, in preparation). Therefore, remote sensing methods that can derive the aerosol radiative forcing with a precision of the order of 1 W m^{-2}, with corresponding changes in optical thickness for optical thicknesses greater than 0.1, are useful for assessing the present aerosol effect.

Due to the growing recognition of the importance of aerosol properties for climate and global change studies, it is indeed fortunate that a number of very significant and much enhanced satellite systems are being developed for launch in the next few years. These sensors will enable the quantitative analysis of tropospheric aerosol optical properties, especially aerosol optical thickness, and will provide additional information on aerosol size distribution, single scattering albedo, and refractive index. They will also provide information on the global distribution, including seasonal and interannual variation, of (i) sources of aerosols (e.g., forest fires, desert dust, and aerosol from oxidation of SO_2 emissions from industrial regions), (ii) aerosol loading and optical properties, (iii) direct radiative forcing (through a combination of spectral and broadband sensors), and (iv) indirect radiative forcing (through a measurement of the change of cloud albedo as aerosol source strengths vary, or by comparing continental and maritime regions in both the Northern and Southern Hemispheres).

The intent of this paper is to describe the various national and international satellite sensors that will enable the remote sensing of tropospheric aerosols from space. These sensors include U.S., Japanese, and European sensors, ranging from the National Oceanic and Atmospheric Administration's (NOAA's) Geostationary Operational Environmental Satellite (GOES), first used for regional aerosol studies in 1980 (Fraser et al. 1984), to the NOAA Advanced Very High Resolution Radiometer (AVHRR), first used for aerosol studies in 1981, and finally to sophisticated sensors being developed as part of NASA's Earth Observing System (EOS), the National Space Development Agency of Japan's (NASDA) ADEOS (Advanced Earth Observing Satellite) series of satellites, and the European Space Agency's (ESA) Envisat-1 program. After briefly outlining the various concepts that have been developed for the determination of the optical, microphysical, and physical properties of aerosol particles, we will summarize the advantages, disadvantages, and unique characteristics of 12 unique satellite sensor systems. The appendix contains the expansions of acronyms used in this paper.

2. Retrieval methods

The shortwave spectral reflectance detected by a satellite radiometer is composed of solar radiation reflected from the earth's surface as well as radiation scattered by the atmosphere in the direction of the sensor. Light reflected from the surface also interacts with the atmosphere, and thus its spectral and angular properties are affected both by the atmosphere and the surface. Light can be scattered to the sensor through single backscattering by an aerosol particle or by a series of forward and/or backward scattering events in the atmosphere. Absorption by gases and aerosol particles is generally spectrally and angularly dependent.

Though aerosol can be located in both the stratosphere and troposphere, stratospheric concentrations are generally quite small. Except following major volcanic eruptions, such as Mount Pinatubo (cf. McCormick et al. 1995), the stratospheric aerosol optical thickness is typically an order of magnitude smaller than the tropospheric optical thickness. It can be assessed and corrected for using limb occultation measurements from the Stratospheric Aerosol and Gas

Experiment (SAGE) (Kent et al. 1995). Some of these measurements can penetrate to the upper troposphere and can thus be used to derive profiles of the aerosol extinction in the upper troposphere.

How do we retrieve aerosol properties from this composite of processes? The diffusely reflected radiation at the top of the atmosphere can be expressed in terms of the reflection function $R(\tau_a, \omega_0; \mu, \mu_0, \phi)$, defined as

$$R(\tau_a, \omega_0; \mu, \mu_0, \phi) = \frac{\pi I(0, -\mu, \phi)}{\mu_0 F_0}. \quad (1)$$

In this expression, $I(0, -\mu, \phi)$ is the reflected intensity (radiance); τ_a the aerosol optical thickness; ω_0 the single scattering albedo (ratio of the scattering optical thickness to the total optical thickness); μ the absolute value of the cosine of the zenith angle θ, measured with respect to the positive τ (downward) direction; ϕ the relative azimuth angle between the direction of propagation of the emerging radiation and the incident solar direction; and μ_0 the cosine of the solar zenith angle θ_0. The functions R, τ_a, ω_0, F_0, and I are all implicitly functions of wavelength λ. This definition of the reflection function, which normalizes the emerging radiance by the incident solar flux F_0, is equivalent to the albedo of the earth–atmosphere system for isotropic radiation.

The reflection function of a cloud-free and vertically homogeneous earth–atmosphere system overlying a Lambertian surface with reflectance A_g can be written as (cf. Chandrasekhar 1960)

$$R(\tau_a, \omega_0; \mu, \mu_0, \phi) = R_{atm}(\tau_a, \omega_0; \mu, \mu_0, \phi) + \frac{A_g}{1 - A_g \bar{r}_{atm}(\tau_a, \omega_0)} \times t_{atm}(\tau_a, \omega_0; \mu) t_{atm}(\tau_a, \omega_0; \mu_0) \quad (2)$$

where $R_{atm}(\tau_a, \omega_0; \mu, \mu_0, \phi)$ is the reflection function, $\bar{r}_{atm}(\tau_a, \omega_0)$ the spherical albedo, and $t_{atm}(\tau_a, \omega_0; \mu_0)$ the total transmission (diffuse plus direct) when $A_g = 0$. Each of these functions is explicitly a function of aerosol optical thickness and single scattering albedo and implicitly a function of aerosol size distribution. In practice, the bidirectional reflectance properties of the surface are substituted for the Lambertian reflectance A_g when applying this expression to satellite observations (Lee and Kaufman 1986).

The relative effects of aerosol optical thickness and single scattering albedo on satellite reflection function measurements is illustrated in Fig. 1, which shows the difference between the reflection function and surface reflectance as a function of surface reflectance for four values of aerosol optical thickness (τ_a = 0.0, 0.2, 0.4, and 0.6) and two values of single scattering albedo (ω_0 = 0.81 and 0.96). This figure is the basis for remote sensing of aerosol optical thickness and single scattering albedo from reflected solar radiation measurements. The maximum sensitivity to aerosol optical thickness occurs over dark surfaces. For surfaces brighter than A_g = 0.1, the sensitivity is much reduced and depends on aerosol absorption. Therefore, measurements over ocean surfaces or dark targets over land are most frequently used to detect aerosol optical thickness from space-based sensors (Griggs 1975) and a combination of dark and bright surfaces are used to detect aerosol single scattering albedo (Kaufman and Joseph 1982).

Measurements of the radiative and microphysical properties of aerosols can be derived using many different methods, including single- and multiple-channel reflectance, multiangle reflectance, contrast reduction, and polarization. A summary of these techniques is outlined below.

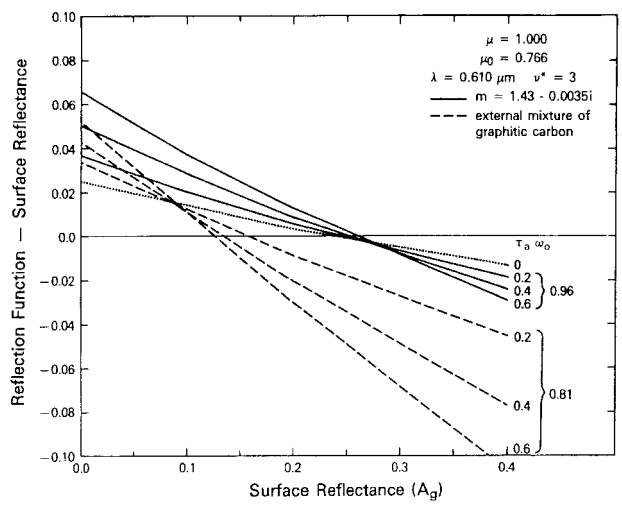

FIG. 1. Difference between the reflection function and surface reflectance at 0.61 μm as a function of surface reflectance for various values of the aerosol optical thickness τ_a and single scattering albedo ω_0. The solid and dashed lines correspond to an aerosol-ladened atmosphere having a Junge size distribution of the form $n(r) \propto r^{-4}$. Results apply to nadir observations (μ = 1) when μ_0 = 0.766 (θ_0 = 40°). For surface reflectance below a given critical value (A_g^c), the aerosol effect is positive (A_g^c = 0.25 for ω_0 = 0.96) and above this value the effect is negative (adapted from Fraser and Kaufman 1985).

a. Single-channel reflectance

An increase in the earth's reflectance is the most distinctive feature in satellite imagery for detecting particulate matter, and has been observed since the earliest days of satellite use. A thick aerosol layer such as from large-scale dust storms or forest fire events can easily be detected by an enhanced reflectance in a visible channel as noted by many investigators (Griggs 1975; Fraser 1976; Mekler et al. 1977; Quenzel and Koepke 1984; Takayama and Takashima 1986; Kaufman et al. 1990a). The NOAA operational one-channel algorithm has been successful at depicting global optical thickness distributions of stratospheric and tropospheric aerosols over the ocean (Stowe et al. 1992; Long and Stowe 1994; Husar et al. 1997). Moulin et al. (1997) recently showed a systematic long-term change in the Saharan dust optical thickness from a 12-yr time series of aerosol optical thickness obtained using a Meteosat one-channel algorithm.

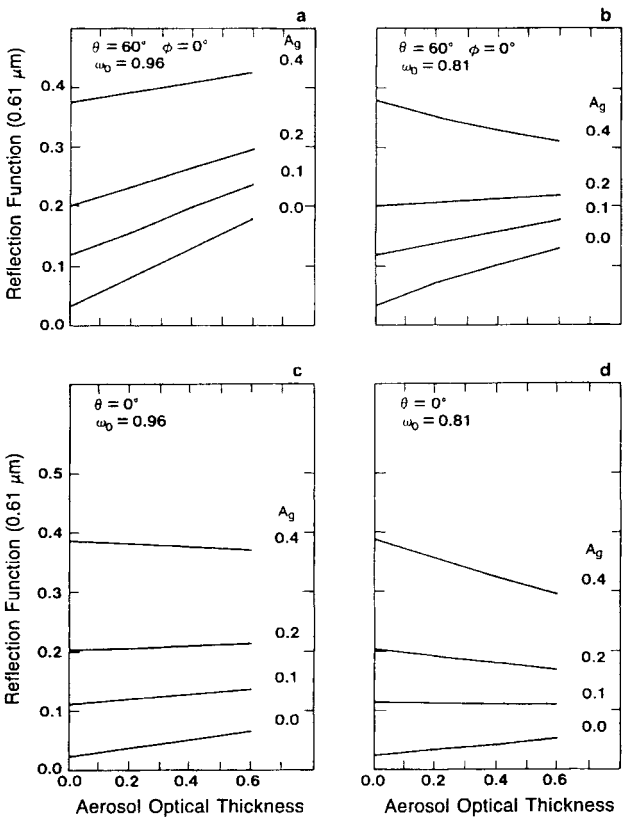

FIG. 2. The reflection function as a function of aerosol optical thickness and surface reflectance for a Junge size distribution given by $n(r) \propto r^{-4}$, where $\lambda = 0.61$ μm and $\theta_0 = 40°$. Panels (a) and (b) apply to $\theta = 60°$ and $\phi = 0°$ but for different single scattering albedos; (c) and (d) to nadir observations ($\theta = 0°$) (adapted from Fraser and Kaufman 1985).

When the surface reflectance is small, the first term on the right-hand side of Eq. (2) dominates, thus yielding sensitivity to the reflection function of the atmosphere alone. This term, in turn, is primarily a function of the aerosol optical thickness with a reduced, though still important, sensitivity to aerosol size distribution and optical properties (i.e., single scattering albedo). Figure 2 illustrates the reflection function at 0.61 μm as a function of aerosol optical thickness for an atmosphere consisting of Rayleigh (molecular) scattering ($\tau_R = 0.066$), ozone absorption ($\tau_{O_3} = 0.021$), and aerosol scattering and absorption, where the aerosol size distribution is assumed to be a Junge distribution of the form $n(r) \propto r^{-4}$ (Fraser and Kaufman 1985). These computations, which include all orders of multiple scattering, apply to $\theta_0 = 40°$ and four different values of the surface reflectance ($A_g = 0.0$, 0.1, 0.2 and 0.4). Figures 2a and 2b show the sensitivity of the reflection function to τ_a and A_g when $\theta = 60°$ and $\phi = 0°$, while Figs. 2c and 2d apply to nadir observations ($\theta = 0°$). Figures 2b and 2d illustrate conditions where the aerosol single scattering albedo $\omega_0 = 0.81$, and contrast sharply with conditions where aerosol absorption is weak ($\omega_0 = 0.96$, Figs. 2a and 2c). This figure clearly illustrates the underlying principle behind the remote sensing of aerosol optical thickness over low reflectance surfaces, namely, the reflection function increases almost linearly as the optical thickness increases, and is the most sensitive for low reflectance surfaces. Figure 2, with its extension to all solar and viewing conditions, can easily be represented in look-up tables (LUTs) that can readily be searched for the aerosol optical thickness that best matches the reflection function observed by a satellite sensor. This is the method that has been implemented in the NOAA operational algorithm described by Stowe et al. (1997).

The physics behind the remote sensing of aerosol optical thickness over a dark target can be understood using the single scattering approximation:

$$R_a \equiv R - R_{mol} - R_g = R_{as'} + O\left(\tau_a^2\right), \qquad (3)$$

$$R_{as'} \equiv \omega_0 \tau_a p_a(\Theta) / \left(4\mu\mu_0\right), \qquad (4)$$

where R_a, R_{mol}, and R_g are the contributions from aerosol scattering, molecular scattering, and surface reflectance, respectively; $p_a(\Theta)$ is the scattering phase function, a function of scattering angle Θ; and $O(\tau_a^2)$ denotes terms of order τ_a^2 or higher. It is, therefore, the

aerosol optical thickness that can be retrieved from the residual in the reflection function, provided one subtracts the effects of molecular scattering and the underlying surface, and that one assumes an appropriate aerosol model. With nonabsorbing aerosols, the linearity between R_a and τ_a is remarkably well maintained, even for large optical thicknesses for which multiple scattering cannot be ignored (cf. Gordon and Wang 1994). In other words, multiple scattering R_{am} is nearly proportional to the linearized single scattering contribution expressed as

$$R_{am} \equiv R_a - R_{as'} \approx cR_{as'} + O\left(R_{as'}^2\right), \qquad (5)$$

where $O(R_{as'}^2)$ denotes terms of order $R_{as'}^2$ or higher. This fact eases the situation of determining the aerosol optical thickness from spaceborne reflected solar radiation measurements. For absorbing aerosols the higher-order dependence on aerosol optical thickness becomes important (cf. Fig. 2). Higurashi and Nakajima (1999) discuss the accuracy of various expansion algorithms for constructing look-up tables required to implement the algorithm defined by Eqs. (3)–(5).

It is essential that one assumes reasonable aerosol optical properties for constraining the problem when using a single-channel algorithm. Most investigators assume spherical particles (Mie scattering) and a Junge power law (Rao et al. 1989), a monomodal size distribution (Kaufman et al. 1990a; Ferrare et al. 1990), or a bimodal size distribution (Tanré et al. 1997; Kaufman et al. 1997a). Assumptions on the aerosol refractive index are also important (Koepke and Quenzel 1981).

The most delicate part of the one channel algorithm for retrieving aerosol optical thickness is subtraction of the surface reflectance signature from the satellite reflectance measurement. Pixels with cone angles, defined as the emergent zenith angle relative to the specular reflection angle, of less than 40° must be omitted for large sun glint regions over the ocean (Stowe et al. 1997). A tilt angle mechanism has been adopted for recent ocean color sensors, such as the Ocean Color and Temperature Scanner (OCTS) and Sea-viewing Wide Field-of-view Sensor (SeaWiFS), in order to increase the cone angle for better coverage of the retrievable region. Whitecap contributions cannot be ignored for surface wind speed above 15 m s^{-1} over the ocean (Koepke 1984). Some algorithms (Rao et al. 1989) use a Lambertian approximation for the underlying surface, which is tuned for the ocean surface; some use a flat ocean surface approximation for multiple scattering contributions (Gordon and Wang 1994; Stowe et al. 1997); others adopt more rigorous boundary conditions of roughened water surfaces (Nakajima and Higurashi 1997; Higurashi and Nakajima 1999; Tanré et al. 1997). Some of these methods are distinctly better than others, and a Lambertian assumption for aerosol retrievals over ocean is not recommended.

Since the aerosol optical thickness is generally less than unity, a good calibration of the radiometer is essential for the successful retrieval of aerosol optical thickness from space (Griggs 1975). With considerable progress in ground-based instrumentation for deriving aerosol optical properties, such as fully automatic sun/sky radiometers, vicarious calibration of satellite-borne radiometers has become more reliable than in the past (Vermote and Kaufman 1995).

b. Multichannel reflectance

Two-channel and multichannel algorithms are promising for extracting not only aerosol optical thickness but also aerosol size distribution information. In two-channel methods the following color ratio is frequently used (Gordon and Wang 1994; Durkee et al. 1986, 1991):

$$\varepsilon_{1,2} = \frac{R_1}{R_2}, \qquad (6)$$

where R_1 and R_2 denote measured reflection functions at wavelengths λ_1 and λ_2, respectively.

From Eqs. (4) and (5) we obtain the following relationship for the color ratio in the single scattering approximation:

$$\varepsilon_{1,2} \approx \frac{\omega_1 \tau_1 P_1(\Theta)}{\omega_2 \tau_2 P_2(\Theta)}. \qquad (7)$$

Durkee et al. (1991) estimated the color ratio as well as the aerosol optical thickness from AVHRR measurements in channel 1 (0.630 μm) and channel 2 (0.830 μm). They found that the color ratio is widely variable over the globe, where they further assumed the two-term Henyey–Greenstein phase function (Kattawar 1975).

Another choice for the index of aerosol color is the Ångström wavelength exponent (α) defined in the expression

$$\tau_\lambda = \tau_{\lambda_0}\left(\frac{\lambda}{\lambda_0}\right)^{-\alpha}, \quad (8)$$

where λ_0 is a reference wavelength (0.5–1.0 μm, depending on sensor). Nakajima and Higurashi (1997) assumed a Mie solution and a power law size distribution to estimate the optical thickness and Ångström exponent from channel 1 and 2 AVHRR radiances. Nakajima and Higurashi (1998) subsequently analyzed both AVHRR and OCTS data assuming a bimodal lognormal size distribution, rather than a power law distribution. The lognormal distribution is more accurate in representing the aerosol size distribution over the globe. Using AVHRR channel 2 radiances, large absorption by water vapor in this relatively broad band easily affects the accuracy of the aerosol retrieval (Ignatov et al. 1998).

There are also methods that have been developed for extracting information on light absorption by aerosols from reflected solar radiation measurements. Suppose aerosol absorption coefficients are largely different at two different channels of a radiometer. The color ratio can thereby be used as an index of single scattering albedo.

Fukushima and Toratani (1997) assumed $\omega_0 = 1$ for channel 4 (0.55 μm) of the Coastal Zone Color Scanner (CZCS) to estimate the single scattering albedo at shorter wavelength channels for Asian dust particles. Asian dust particles have strong absorption in the blue channel. In an analogous manner, J. R. Herman et al. (1997) defined the following index for UV absorbing aerosols:

$$\Delta N = -100\log_{10}\left[\left(\frac{R_{340}}{R_{380}}\right)_{\text{obs}} - \left(\frac{R_{340}}{R_{380}}\right)_{\text{cal}}\right], \quad (9)$$

where they compared the observed color ratio between the 340- and 380-nm channels of the Total Ozone Mapping Spectrometer (TOMS) with that calculated with the assumption that there is no change in absorptivity between 340 and 380 nm. In this application, cloud contamination is less important, in spite of the fact that TOMS has a large instantaneous field of view (40 km), since cloud reflectance does not depend strongly on wavelength. Clouds do, however, have some impact on aerosol retrievals by virtue of being primarily above the majority of the tropospheric aerosol.

Multichannel reflectance algorithms for retrieving aerosol optical properties both over ocean and land surfaces have been developed and tested for various satellite sensors currently in operation, examples of which will be shown in section 5 (below). These retrievals can be much improved for the next generation of satellite imagers such as the Moderate Resolution Imaging Spectroradiometer (MODIS) and Global Imager (GLI) due in part to the enhanced number of narrow and well-chosen spectral channels and an improved ability to diagnose and identify clouds in the field of view of the radiometer. Tanré et al. (1997) have adopted the characteristic component method that consists of selecting a reasonable combination of aerosol size modes and concentrations from a prescribed library of physical aerosol models.

c. Dark targets over dense, dark vegetation

Green vegetation, and some soils, are dark in the red (0.6–0.7 μm) and blue (0.4–0.5 μm) spectral regions. Mixed vegetation and soils can be dark or bright depending on the fraction of vegetation cover, vegetation greenness, and soil optical properties. In order to estimate the aerosol optical thickness over land, the surface reflectance of these dark pixels must be estimated to an uncertainty ΔA_g = 0.005–0.01. This uncertainty translates to an error in optical thickness of 0.05–0.10. We therefore need a method to assess the surface reflectance through an aerosol layer of unknown optical thickness. To overcome this uncertainty due to aerosol–surface interaction, it is necessary to incorporate an additional dimension to the problem, namely, the spectral dimension whereby the surface is observed at a wavelength for which minimal aerosol contamination occurs.

This method of deriving aerosol optical thickness over dark targets and dense dark vegetation can be understood as follows. First, with the exception of dust, the aerosol optical thickness typically decreases with wavelength according to Eq. (8), where $1 \le \alpha \le 2$ (Kaufman 1993). Therefore τ_a is 3–30 times smaller in the shortwave-infrared (SWIR; 2–4 μm) region than in the visible (0.47 and 0.66 μm). Second, surface reflectance across the solar spectrum is well correlated. Soils usually have a reflectance that increases as a function of wavelength, with a correlation that slowly decreases as the wavelength span increases (Kaufman et al. 1997b). Parallel processes affect the surface reflectance between 0.47 and 0.66 μm and between 2.1 and 3.8 μm. Vegetation decreases the reflectivity in the visible region due to chlorophyll absorption and in the

SWIR region due to absorption by liquid water. Wet soil has a lower reflectance in the visible region due to trapping of light, and in the 2.1- and 3.8-μm regions due to liquid water absorption. Surface roughness, shadows, and inclinations decrease the reflectance across the entire solar spectrum (Kaufman and Remer 1994; Kaufman et al. 1997b).

Figure 3 shows an example of the relationship between surface reflectance at 0.49 and 0.66 μm, compared to that at 2.2 μm. The brighter surface reflection at 2.2 μm, and the overall smaller aerosol single scattering albedo at longer wavelengths (Hobbs et al. 1997; Eck et al. 1998), decrease further the aerosol effect on the detected radiance at this wavelength. Therefore the effect of aerosol (smoke and urban/industrial aerosol but not dust) is expected to be 15–30 times smaller in the SWIR (2.1 or 3.8 μm) than in the visible (0.47 and 0.66 μm) and can, therefore, be neglected.

The MODIS operational algorithm for the remote sensing of aerosol over land is an example of the application of these principles. Surface targets that are expected to be dark in the visible channels (0.47 and 0.66 μm) are determined using the 2.1- or 3.8-μm channels. MODIS uses a cascade of thresholds, starting with $A_g(2.1\ \mu\text{m}) = 0.05$, followed by $A_g(3.8\ \mu\text{m}) = 0.025$, and finally $A_g(2.1\ \mu\text{m}) = 0.10$ if too few pixels made the 3.8-μm threshold (Holben et al. 1992; Kaufman et al. 1997a). The 3.8-μm threshold corresponds to the lowest reflectance in the visible, for example, dense dark green forest, but suffers from uncertainty in the correction for thermal emission and therefore is selected as the second choice. The 2.1-μm thresholds extend the technique to partial vegetation cover or grasslands that are partially green. The corresponding reflectance in the visible is estimated as follows:

$$A_g(0.47\ \mu\text{m}) = 0.5A_g(0.66\ \mu\text{m}) = 0.25A_g(2.1\ \mu\text{m}), \quad (10)$$

when $A_g(2.1\ \mu\text{m}) \le 0.05$. If this criterion is not met, a second, slightly less accurate, criterion is used to estimate surface reflectance:

$$A_g(0.47\ \mu\text{m}) = 0.5A_g(0.66\ \mu\text{m}) = 0.01, \quad (11)$$

when $A_g(3.8\ \mu\text{m}) \le 0.025$. Finally, if neither criterion is satisfied, a third criterion is tested that is the same as Eq. (10), but used when $A_g(2.1\ \mu\text{m}) \le 0.10$. These simple relationships, incorporated into the operational MODIS algorithm for remote sensing of aerosol optical thickness over vegetated land surfaces, is currently being examined as a function of observational viewing conditions using measured bidirectional reflectance measurements (Tsay et al. 1998; Soulen et al. 1999*;* Arnold et al. 1999, manuscript submitted to *Int. J. Remote Sens.*).

The aerosol optical thickness is derived from the difference between the apparent reflectance at the top of the atmosphere, R, and the surface reflectance A_g. This difference, the aerosol signal, is available in the blue and red channels. The spectral dependence of the aerosol signal can be used to derive the ratio between the influence of coarse particles (e.g., dust) and accumulation mode particles (e.g., smoke or urban/industrial pollution). This spectral information is used in the following manner. First, a given aerosol model is assumed in order to derive an estimate of the optical thickness and of the surface component in R [second term on the right-hand side of Eq. (2)]. This term is subtracted from R and the spectral path radiance, R_{atm}, is obtained. The ratio of R_{atm} between the blue and the red channel is used to estimate the aerosol model and thus to derive the correct aerosol optical thickness. A high ratio corresponds to a dominance of small particles and a small ratio to a dominance of coarse particles. Though the derivation of path radiance using this technique does not depend significantly on the assumed aerosol model, this procedure is new.

This retrieval algorithm for remote sensing of aerosol optical thickness over dark land surfaces will first

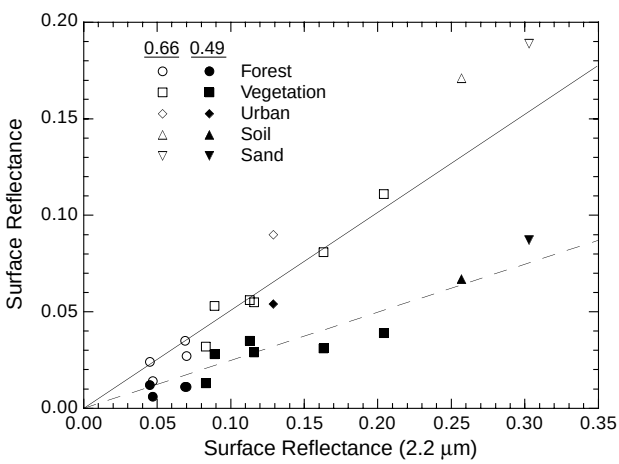

FIG. 3. Scatter diagram between the surface reflectance at 0.49 μm (solid symbols) and 0.66 μm (open symbols) to that at 2.2 μm, for several surface types. The average relationships $A_{0.49}/A_{2.2} = 0.25$ and $A_{0.66}/A_{2.2} = 0.5$ are also plotted (dashed and solid lines, respectively) (adapted from Kaufman et al. 1997b).

be applied to global satellite observations following the launch of MODIS on the Terra spacecraft in late-1999. In testing this algorithm using data from the MODIS Airborne Simulator (MAS) (King et al. 1996) aboard the NASA ER-2 aircraft, two possible sources of error have been identified: (i) inland turbid, subpixel water bodies that may be dark enough in the SWIR but more reflective than anticipated in the visible, and (ii) subpixel snow and ice, where the snow is relatively dark in the SWIR but quite reflective in the visible. A few percent of subpixel snow cover may generate large errors in the estimation of surface reflectance in the visible channels and hence in the derived optical thickness.

To overcome these problems in the MODIS algorithm, several provisions have been implemented. The main one is a careful selection of dark pixels with which to apply the algorithm, and is based on the finding that most sources of contamination tend to generate higher optical thickness. On a grid of 20×20 pixels (10 km $\times$ 10 km at nadir), the selected dark pixels are sorted as a function of reflectance in the blue and red, and only the average of the 10th to 40th percentiles is used in each band, respectively, in the derivation of aerosol optical thickness. In this way, even if 60% of the dark pixels are contaminated by turbid water or snow, they will not affect the derived aerosol optical thickness. Shadows in the field of view of the radiometer are identified as an essential component of the cloud mask algorithm that is run prior to the application of the aerosol optical thickness retrieval (King et al. 1998; Ackerman et al. 1998), and are therefore not a significant source of error for MODIS.

The original application of the dark target approach to aerosol remote sensing over land was to Landsat 3 Multispectral Scanner (MSS) data that do not have SWIR channels (Kaufman and Sendra 1988). It was based on detecting green forests using dark pixels derived from the normalized difference vegetation index (NDVI) and reflectance at 0.86 μm. Dark vegetation was determined by a combination of high NDVI and low reflectance. For these pixels, the reflectance in the red channel is assumed to be $A_g(0.66\ \mu\text{m}) = 0.02 \pm 0.01$ and used to derive the aerosol optical thickness, resulting in a very good agreement with sunphotometer measurements in the mid-Atlantic region of the United States (Kaufman and Sendra 1988). Determination of dark pixels using the vegetation index is, however, affected by the sensitivity of the vegetation index itself to aerosols. To avoid this feedback loop the method was applied only to images for which it was known a priori that dense vegetation pixels were present in the image (Soufflet et al. 1997). The multiangle data to be obtained from the Multi-angle Imaging Spectroradiometer (MISR) instrument, discussed later in this paper, also do not have SWIR channels. MISR does plan, however, to use a similar technique for identification of dark pixels, though, as will be shown later, they take advantage of the multiangle observations to circumvent this feedback loop.

This is illustrated in Airborne Visible and Infrared Imaging Spectrometer (AVIRIS) (Vane et al. 1993) images acquired on 25 August 1995 near Cuiabá, Brazil, when $\theta_0 = 28.7°$ (Fig. 4). Figure 4a was constructed from a red–green–blue composite of 0.66-, 0.55-, and 0.46-μm images, while Figs. 4b–d show images for individual bands at 0.46, 0.66, and 2.13 μm. For all individual bands, the images were stretched over a fixed grayscale from $0.0 \le R \le 0.3$, showing not only the decreasing influence of aerosol optical thickness as the wavelength increases, but also the increasing reflectance of land surfaces at 2.13 μm relative to that at 0.46 and 0.66 μm (discussed in the previous subsection). The smoke is seen primarily at the shortest two wavelengths, and fire and bright land at 2.13 μm. This figure demonstrates how the 2.13-μm image, which is largely free of any smoke aerosol effect, can be used to detect surface features and predict their reflectance at 0.46 and 0.66 μm.

The dense dark vegetation mask was also run on this scene (Fig. 4e), where all pixels for which the surface reflectance $A_g(2.13\ \mu\text{m}) \le 0.10$ are shown in green and pixels for which $0.10 < A_g(2.13\ \mu\text{m}) \le 0.15$ are shown in yellow. The background image on which the dark vegetation pixels are overlaid is the AVIRIS image at 0.86 μm, for which vegetation is bright and burn scars dark. A second criterion, $A_g(0.86\ \mu\text{m}) > 0.10$, was also applied to assure that water and burn scars were eliminated as dense dark vegetation surfaces.

d. Reduction in contrast over land

As noted above, pixels covered by dense dark vegetation (DDV) are very suitable for interpreting the satellite signal in terms of an atmospheric contribution, but, unfortunately, there are regions where very dark pixels do not exist and where the method cannot be applied. In addition, there are regions such as the Sahara and Sahelian regions of Africa, where the surface albedo is close to the critical value, defined as the surface reflectance for which the radiance at the top of the atmosphere is not directly related to the aerosol optical thickness (cf. Fig. 1). As a consequence, alter-

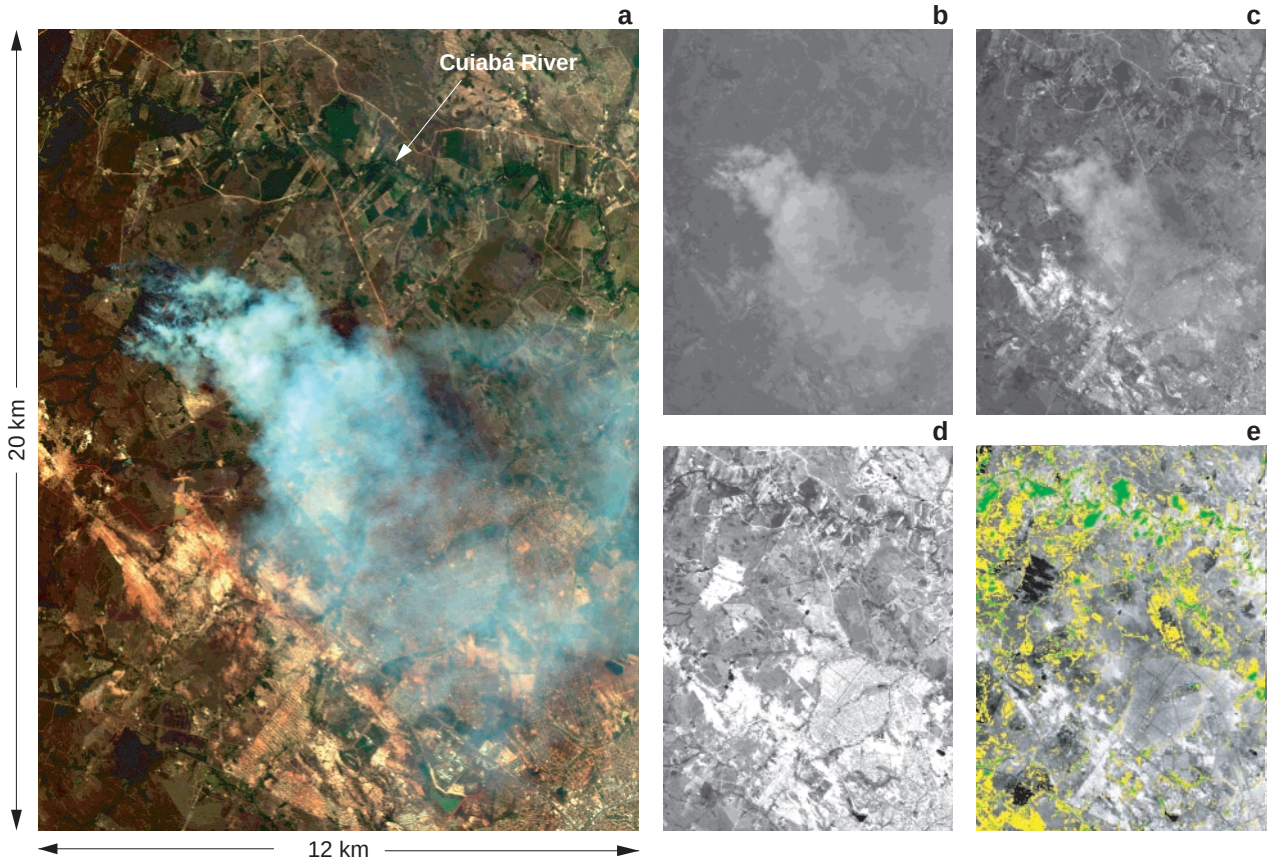

FIG. 4. AVIRIS images acquired near Cuiabá, Brazil, on 25 Aug 1995. (a) A red–green–blue composite of 0.66, 0.55, and 0.46 μm bands; (b)–(d) images for individual bands. Panel (b) applies to 0.46 μm, which is especially sensitive to smoke, (c) to 0.66 μm, also sensitive to smoke but with brighter surface reflectance, and (d) to 2.13 μm, which shows both hot ground and bright land. (e) Location of all dense dark vegetation within this scene, defined as pixels for which the surface reflectance $A_g(2.13\ \mu\text{m}) \le 0.10$ (green pixels) or $0.10 < A_g(2.13\ \mu\text{m}) \le 0.15$ (yellow pixels). The background image on which the dark vegetation pixels are overlaid is the AVIRIS image at 0.86 μm, for which vegetation is bright and burn scars dark.

native methods, such as contrast reduction, have been developed. This method is still being investigated, and thus it is difficult to draw final conclusions on its applicability on a global scale. Nevertheless, preliminary results are quite promising and hence it is worth exploring further.

Schematically, the method is based primarily on the second term on the right-hand side of Eq. (2), unlike the DDV approach that is based primarily on the first term. Briefly, the difference in reflection function ΔR_{ij} between two adjacent pixels i and j (called contrast) decreases as the optical thickness increases. It can be related to the actual ground reflectance difference $\Delta A_g^{ij} = A_g^i - A_g^j$ by

$$\Delta R_{ij}(\tau_a, \omega_0; \mu, \mu_0, \phi) = \Delta A_g^{ij}\, t_{atm}(\tau_a, \omega_0; \mu) \times t_{atm}(\tau_a, \omega_0; \mu_0). \quad (12)$$

Provided the ground reflectance features (ΔA_g^{ij}) can be determined, the transmission function $t_{atm}(\tau_a, \omega_0; \mu)$ $t_{atm}(\tau_a, \omega_0; \mu_0)$ can be derived from the satellite measurements and then related to aerosol optical thickness. Therefore, the determination of ΔA_g^{ij} is a necessary condition for the application of this technique. For this reason, the method has only been applied to groups of images. If one of these images was obtained on a clear day, the actual ground reflectance difference ΔA_g^{ij} can be estimated and, as long as the surface target is invariant, variations in the transmission function can be attributed to variations in the aerosol content. The selection of a clear day from a sequence of satellite images is itself not an easy task and has, therefore, been based on visual inspection of the "sharpness" of the image. More rational, ground optical thickness measurements can be performed for a day and this specific day used as the reference clear

day for a group of images; results can then be scaled accordingly. Since ΔA_g^{ij} may be affected by surface bidirectional reflectance characteristics, the determination of τ_a has to be made for a pair of images with similar viewing conditions, when bidirectional reflectance effects are ignored. With the advent of MODIS, MISR, and POLDER (Polarization and Directionality of the Earth's Reflectances), surface bidirectional reflectance will be derived to a much higher degree of accuracy than in the past, thereby allowing the reduction in contrast method to be extended to any geometrical condition.

This method has been successfully applied to Thematic Mapper (TM) (Tanré et al. 1988) and AVHRR (Holben et al. 1992) images taken over arid regions where the concept of an invariant target is largely valid. Figure 4b clearly points out the reduction in contrast that occurs when the optical thickness increases from smoke-free to smoke-filled regions. This was also demonstrated by observations of optical thickness in smoke-free regions using nearly simultaneous ground-based sunphotometer measurements. Also, results of sunphotometer measurements showed that $\tau_a(0.46\ \mu\text{m}) = 0.30$, decreasing to $\tau_a(0.86\ \mu\text{m}) = 0.10$. In the upper part of these images there is a riverbed that emphasizes the relationship between the wavelengths. This riverbed, identified in Fig. 4a, is dark at 0.66 and 2.13 μm.

The optical thickness derivation depends on the single scattering albedo and asymmetry parameter but is largely independent of aerosol phase function, since the total transmission function $\tau_{atm}(\tau_a, \omega_0; \mu_0)$ has little sensitivity to details of the single scattering phase function. The reduction in contrast is also a function of the instantaneous field of view of the sensor. The sensitivity of the transmission function to optical thickness is larger for higher spatial resolution data, since only photons directly transmitted to the sensor contribute appreciably to the reflected solar radiation signal (Tanré and Legrand 1991). For example, the contrast reduction is 40% lower for the AVHRR resolution (1 km) than for TM resolution (30 m), but is still large enough to be applied to hazy or dusty conditions where large variations in the aerosol content are expected.

The remaining problem is the determination of the invariant target from satellite observations. Progress in this aspect is currently being made. In particular, a procedure based on the structure function derived from the satellite image itself has been developed to determine whether conditions for applying the method are met (Holben et al. 1992; Tanré et al. 1992). The procedure needs to be applied to more cases before it can be concluded that the concept is widely applicable.

e. Thermal contrast

An early study (Shenk and Curran 1974) showed the potential of using thermal infrared data to detect Saharan dust over land. More recent studies have shown that the Meteosat infrared channel (10.5–12.5 μm) (Legrand et al. 1988), as well as the 3.7- and 11-μm channels of AVHRR (Ackerman 1989), are affected by the presence of dust and that quantitative estimates of the aerosol optical thickness are possible using brightness temperature differences between 8.5, 11, and 12 μm (Legrand et al. 1989; Ackerman 1997).

This method is based on observing outgoing thermal radiation (10–12 μm) emitted by the same scene over the course of several days, during which time the aerosol content of the atmosphere has changed. The principal assumptions behind this method are (i) the radiance emitted by the surface is constant or linearly varying over the time period of the observations, and (ii) one of the days is aerosol free. In the presence of aerosols, the outgoing longwave radiation is attenuated along its path through the aerosol layer, resulting in a reduction in outgoing longwave radiation when compared to a clear day. Furthermore, the solar flux available to heat the surface is reduced by the presence of aerosols due to enhanced scattering of shortwave radiation, which in turn leads to a drop in the surface temperature. Both of these effects reduce the thermal infrared radiation emitted to space, thereby increasing the contrast between observations obtained during clear and hazy conditions. This thermal contrast can in turn be related to aerosol content.

Obviously, this method works best when aerosols have an impact in the thermal infrared, and it is for this reason that it has been applied solely to the case of Saharan dust. Since the spectral optical thickness of most aerosol layers varies according to Eq. (8) with $1 \le \alpha \le 2$, it is almost negligible in the thermal infrared window region (10.5–12.5 μm). This is not the case for dust that, due to the presence of large particles, has an optical thickness that is quite appreciable in the thermal infrared. In addition, in arid and semiarid regions, the surface temperature is generally high and the relative humidity low, which leads in turn to sufficient thermal contrast to enable the aerosol optical thickness to be inferred.

This concept is illustrated in Fig. 5, adapted from Legrand et al. (1988). It shows the temporal variation

of surface temperature measured by thermocouples at a location near the Niamey airport, Niger, during the Etude de la Couche Limité Atmosphérique Tropical Sèche (ECLATS) experiment for clear and dusty conditions. The dusty days were selected from days having ground visibility measured at the airport of less than 10 km. During the daytime, since there is less solar energy reaching the surface due to the presence of dust, there is a decrease of about 2°C in the surface temperature. At nighttime, the presence of dust reduces the diurnal temperature range because the aerosol layer acts like a greenhouse gas. The impact of dust is less at night than during the daytime, with an increase of about 1°C being all that is observed.

From space, because of the additional attenuation through the aerosol layer, very large reductions in brightness temperature of up to 25°C have been observed during the day in the 10.5–12.5-μm channel of Meteosat for major dust events. Usually, the reduction in the brightness temperature decrease at night is typically half as large as the daytime decrease. A quantitative comparison of satellite data with ground photometric measurements in Niamey, Niger (Legrand et al. 1989), and in M'Bour, Sénégal (Tanré and Legrand 1991), have demonstrated the capability of this method to derive aerosol optical thickness over desert environments.

There are other effects that can affect the thermal infrared radiance detected by a satellite, namely, the water vapor content, surface winds, or presence of clouds. Assuming the images are correctly cloud screened, the variations of satellite radiance can empirically be accounted for by variations in the aerosol content and atmospheric moisture alone; other atmospheric parameters, like winds and boundary layer height, do not have a significant impact on the measurements. Moreover, the possible feedback effects that could be introduced by cloudiness are not detectable (Legrand et al. 1989). There is also the annual cycle of surface heating due to variations in the solar illumination, but this effect can easily be accounted for (Legrand et al. 1989).

Finally, the sensitivity of the infrared radiance to variations in water vapor content is comparable to variations induced by the presence of dust; a variation $\Delta u = 1$ g cm^{-2} in the precipitable water corresponds to a variation $\Delta\tau_a(0.55\ \mu\text{m}) = 1$ (Tanré and Legrand 1991). Therefore, the determination of precipitable water is required for application of this technique to sites where the atmospheric moisture has significant day-to-day fluctuations. Several satellite sensors, such as MODIS (Kaufman and Gao 1992) and POLDER (Bouffies et al. 1997), are able to derive this parameter over land from space on a global scale.

f. Land–ocean contrast

While the satellite-detected radiance for low surface reflectance depends primarily on aerosol optical thickness and single scattering phase function, the dependence of radiance on surface reflectance is affected primarily by the aerosol single scattering albedo (cf. Fig. 1). Therefore measurements of the radiance for two contrasting surface reflectances and for two different aerosol loadings (a "clear" and a "hazy" day are required) can be used to derive the aerosol single scattering albedo (Fraser and Kaufman 1985). Such contrast methods have been applied to high-resolution satellite images (MSS; 80 m) between two different surface types (e.g., a seashore). The aerosol single scattering albedo and optical thickness can then be derived simultaneously (Kaufman and Joseph 1982). A similar method has been applied to 1-km AVHRR data for smoke and industrial pollution (Kaufman 1987).

A sensitivity study shows that the aerosol single scattering albedo can be derived with an error of ±0.05. The error can be much smaller for larger aerosol loading over bright land if the size distribution is well known. Validation of this technique is difficult because columnar in situ measurements of aerosol absorption are not readily available. Since the derivation of single scattering albedo depends on particle size, and particle size can be retrieved from spectral reflec-

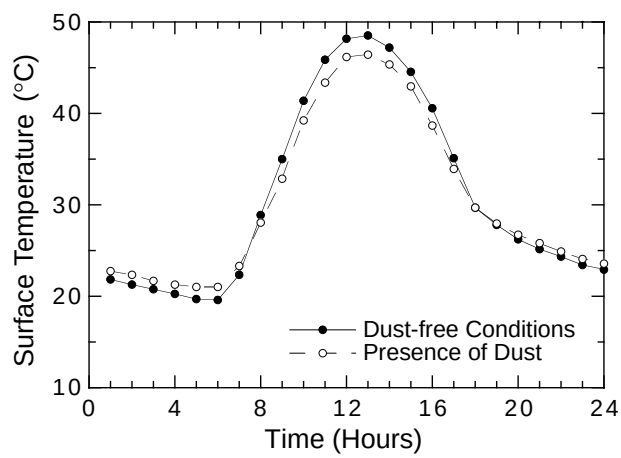

FIG. 5. Temporal variation of surface temperature measured by thermocouples near the Niamey airport, Niger, during the ECLATS experiment for both clear and dusty conditions. The dusty days have been selected when the ground visibility measured at the airport was less than 10 km (adapted from Legrand et al. 1989).

tance measurements over the water, an iterative method for simultaneous remote sensing of aerosol optical thickness, single scattering albedo, and effective particle size was developed (Kaufman et al. 1990a). This method was then applied to AVHRR data containing smoke from a large fire in Canada that spread across the eastern United States (Ferrare et al. 1990). In this iterative scheme the particle size was first derived from the spectral radiance over the water and subsequently used to derive the single scattering albedo from the land–water contrast and optical thickness from the reflected radiance over the water and dark land surfaces. Since, in order to derive particle size, it is first necessary to assume values of optical thickness and single scattering albedo, a second or third iteration may be required in order to adjust the initial assumptions. This method can be significantly improved if, instead of the two visible and relatively broadband AVHRR channels, together with uncertain water vapor absorption properties, a wider range of narrowband channels is used, such as will be available on MODIS and GLI.

g. Angular distribution of reflectance

Remote sensing of aerosol over land using a single view direction, as is common practice for the vast majority of satellite sensors, has limited information content even when a large number of spectral bands are available. Over ocean, a wide spectral range, such as available on MODIS and GLI, can be used to derive the aerosol size distribution quite successfully. Over land, on the other hand, the surface is dark at typically two nearby spectral bands (red and blue) which does not permit such detailed inversion to be performed. Recently, remote sensing of aerosol properties from space has been enhanced by the development of four new satellite sensors, all of which use multiangle measurement strategies to increase the information content of satellite data over both land and ocean.

On the ADEOS spacecraft, launched in August 1996, POLDER (Deschamps et al. 1994) provided observations of the same location on the earth's surface at multiple observation angles, albeit for a limited spectral range (0.44–0.91 μm) and only at moderate spatial resolution (6 km $\times$ 7 km). It also included, for the first time, measurements of polarization at three of its eight spectral bands. Remote sensing over land from POLDER emphasizes the use of polarization and is discussed later in this section. On Terra, the MISR, scheduled for launch in 1999, will provide routine global multiangle observations of the earth using arrays of detectors. Though also restricted in spectral coverage (four bands between 0.44 and 0.86 μm), it views the earth from nine different view directions, including nadir, four forward directions and four aft directions along the spacecraft track (Diner et al. 1989). The Along-Track Scanning Radiometer-2 (ATSR-2) aboard the second Earth Remote Sensing satellite (*ERS-2*) has seven spectral bands that simultaneously view nadir and 55° forward of the velocity vector of the spacecraft (Veefkind and de Leeuw 1997; Veefkind et al. 1999). In this case, the four bands used for aerosol remote sensing are 0.56, 0.66, 0.87, and 1.6 μm, all of which have a spatial resolution of 1 km. The Earth Observing Scanning Polarimeter (EOSP), designed for launch on the second EOS AM platform in 2004, takes advantage of a fuller spectral coverage (0.41–2.25 μm), together with polarization and along-track angular information, but only for a single pixel swath along track. EOSP replaces global coverage acquired over 6–9 days with powerful statistical information. To demonstrate the use of angular information, we review here the algorithms used for MISR and ATSR-2, since they do not make use of polarization.

Martonchik and Diner (1992) developed an algorithm for deriving aerosol optical properties using MISR multiangle observations. Over land the algorithm uses two distinct pathways. If dense vegetation is present, the algorithm uses the low reflectance of dense vegetation, together with multiangle measurements, to derive aerosol optical thickness and the best fitting aerosol model. If dense vegetation pixels are absent, the algorithm uses the angular dependence of spectral contrasts in the reflection function measurements to determine the aerosol optical thickness and aerosol model.

In a similar fashion to Kaufman and Sendra (1988), the MISR approach uses the vegetation index to determine the pixels in the image that correspond to dense dark vegetation. With the help of the angular dependence of vegetation index, however, the MISR algorithm avoids the feedback between vegetation index and aerosol opacity that was encountered by Kaufman and Sendra (1988). The detection of dark pixels is based on the assumption that the vegetation index is more influenced by atmospheric effects than by any uncertainty in the angular dependence of the vegetation index, an assumption that is valid as long as the view direction is not too great (Martonchik 1997). An analytical function is fit to the dependence of vegetation index on air mass ($1/\mu$), using both forward- and

aft-viewing cameras. Since the slant optical thickness is proportional to air mass, the slope of this function is used to extrapolate the vegetation index to a hypothetical value of $1/\mu = 0$, corresponding to no atmospheric effect. This is analogous to Langley plot methods of deriving aerosol optical thickness from ground-based sunphotometers. An average value of the extrapolation in the forward and backward directions is used to further reduce the residual effects of any angular dependence of surface reflectance. For these pixels, a given bidirectional reflectance function is assumed and, together with the measured angular and spectral radiance, used to determine the aerosol optical thickness in all spectral bands for which vegetation is dark. Through this process an appropriate aerosol model that describes the scattering phase function and spectral single scattering albedo is determined from the angular dependence of reflected radiance. Over oceans, the multiangle pointing enables the derivation of the angular dependence of the aerosol scattering phase function if the along-track direction is close to the principal plane (Wang and Gordon 1994), provided one excludes angles close to the direction of sun glint. This information is sufficiently accurate to enable aerosol nonspherical scattering properties to be determined (Kahn et al. 1997).

For ATSR-2, and later for the Advanced Along-Track Scanning Radiometer (AATSR) to be flown on Envisat-1 in 2000, aerosol optical thickness is retrieved separately for nadir and off-nadir measurements and the subsequent results intercompared (Veefkind and de Leeuw 1997). The spectral radiance is inverted using an LUT for two aerosol types, anthropogenic and sea-salt aerosol, based on the Navy Oceanic Vertical Aerosol Model (Gathman and Davidson 1993). The LUT was generated for $\tau_a = 0.0$ and 0.1, and the inversion optimized by fitting the four spectral radiances with two free parameters (η, κ) from a mixing model as follows:

$$R = R_{\text{mol}} + \kappa[\eta R_{\text{anth}} + (1 - \eta)R_{\text{sea}}]. \qquad (13)$$

This is based on the Wang and Gordon (1994) composition approximation and their findings that the exact roles of each aerosol type on the composition is not important as long as one of the modes does not have ω_0 significantly less than the other. It is also based on a linear dependence of the radiance on aerosol optical thickness for small optical thicknesses (cf. Fig. 2). This approach has been applied to the Southern Hemisphere quite successfully. Comparisons between the results for the nadir and off-nadir views show that for the South Atlantic and South Pacific, the results agree to within $\Delta\tau_a(0.56\ \mu\text{m}) = \pm 0.01$ ($\tau_a = 0.08$). For the southern Indian Ocean the two agree to within $\Delta\tau_a(0.56\ \mu\text{m}) = \pm 0.02$ ($\tau_a = 0.11$).

h. Polarization

The principle behind the use of polarization for the remote sensing of aerosol properties from space is the extreme sensitivity that polarization has to the microphysical properties of the aerosol particles, especially the effective particle radius and refractive index. When used in combination with the total reflection function, either at one or multiple view angles (as with POLDER and EOSP), there is nearly a complete orthogonality in the simultaneous retrieval of aerosol optical thickness and effective radius r_e, thereby leading to a much more accurate solution for both parameters (cf. Mishchenko and Travis 1997). Further advantages of polarization include the fact that polarized radiance (Q) is less sensitive to surface reflectance than total radiance (I) alone, as shown in section 5.

For EOSP, which measures three elements of the Stokes vector (I, Q, and U) at 12 wavelengths while scanning ±65° along track, the following two criteria are used simultaneously to determine aerosol optical thickness and effective radius:

$$\frac{|I_{\text{meas}} - I_{\text{calc}}|}{I_{\text{calc}}} \le 0.04 \qquad (14)$$

and

$$\frac{1}{2}\left(|q_{\text{meas}} - q_{\text{calc}}| + |u_{\text{meas}} - u_{\text{calc}}|\right) \le 0.002, \qquad (15)$$

where $q = Q/I$, $u = U/I$, and the indices "meas" and "calc" denote measured and calculated (look-up table) models, respectively. Mishchenko and Travis (1997) showed that Eq. (14), the traditional approach for single-channel, single look-angle retrievals (e.g., AVHRR), leads to ambiguous solutions for τ_a and r_e. In contrast, Eq. (15) leads to very accurate retrievals of r_e and a much-improved retrieval of τ_a. Finally, when used together, errors in optical thickness of $\Delta\tau_a = \pm 0.015$, effective radius of $\Delta r_e = \pm 0.03\ \mu$m, and the real part of the refractive index of $\Delta n = \pm 0.01$ appear possible.

The value of polarization for the quantitative remote sensing of aerosol properties from space has been

demonstrated using POLDER data. This technique is nevertheless hampered by two primary difficulties: (i) the polarization properties of realistic aerosols, many of which are nonspherical and inhomogeneous, may differ from simple models of homogeneous spherical particles, and (ii) the underlying ground surface is itself polarized, and must therefore be characterized and removed from the satellite signal. Both of these concerns have been carefully examined and discussed by M. Herman et al. (1997), who show that polarized light is much more sensitive to the radiative properties of aerosols than to the surface, especially over vegetation. The operational algorithm used by POLDER to determine surface and aerosol properties is described by Leroy et al. (1997). With the relatively large spatial resolution of POLDER (6 km × 7 km) and EOSP (10 km), coupled with the lack of thermal channels, the first problem in applying these data to routine analysis of aerosol properties from space is the determination of a cloud mask that distinguishes the clear, unobstructed scenes to which the algorithm may be applied.

3. Aerosol models

Once the surface reflectance properties have been accounted for, the optical thickness can be derived from the measured radiance and/or polarization using one of the many techniques outlined in the previous section, provided the necessary supplemental information on aerosol properties is available, namely, the aerosol scattering phase function and single scattering albedo. This means that a single view of a given pixel over land cannot be used to identify these aerosol optical properties unambiguously, and hence they have to be assumed based on the best possible aerosol model.

The aerosol single scattering albedo and phase function are typically estimated from aerosol climatology for a given location. The aerosol climatology that has most frequently been used is that compiled by d'Almeida et al. (1991). It includes average properties of the dominant type of tropospheric aerosols as a function of latitude, longitude, and season. Since most measurements of aerosol size distribution are obtained at the ground or using in situ observations from aircraft, they do not typically represent the whole atmospheric column or the ambient aerosol. Over ocean, for example, even though the aerosol size is being retrieved, the possible selection of aerosol size distribution has to be restricted using available aerosol models (Tanré et al. 1997).

The main uncertainty affecting remote sensing of tropospheric aerosols is the uncertainty in the aerosol size distribution, single scattering albedo, and corresponding single scattering phase function. Therefore, an extensive aerosol robotic network (AERONET; Holben et al. 1998) of autonomous sun/sky radiometers was deployed in Brazil during intense biomass burning periods (Holben et al. 1996), in Africa and Israel during dust events, and in the eastern United States in the presence of industrial and urban pollution (Remer et al. 1996). The aerosol properties retrieved from these optical thickness and sky radiance measurements include the spectral optical thickness, aerosol size distribution, phase function, and single scattering albedo (King et al. 1978; Nakajima et al. 1986; Kaufman et al. 1994; Dubovik et al. 1998). These results have been used to derive a new climatology for the columnar aerosol size distribution.

Results of this analysis for urban/industrial aerosol from the mid-Atlantic of the United States and for biomass burning aerosol from Brazil are summarized by Remer et al. (1996). Analysis of the size distribution shows that part of the variability in the particle size can be stratified as a function of aerosol optical thickness (cf. Fig. 6). This stratification is an advantage for remote sensing of aerosol from space, since for any aerosol optical thickness an appropriate size distribution can be used. For the urban/industrial aerosol, 60% of the variance is accounted for by variations in optical thickness, where the high optical thickness corresponds to hazy stagnant air that has had time to age through cloud processes and thus to increase in size (Hoppel et al. 1990; Kaufman et al. 1997a). It also corresponds to higher humidity conditions that act to increase the particle size. Biomass burning aerosol, on the other hand, does not show any regular dependence of particle size on optical thickness, due presumably to the fact that these particles are emitted during the dry season, have low humidity, are generated a short time after the smoke leaves the fire, and the cloud fraction is low.

A combination of this dynamic model, together with single scattering albedo and refractive index derived from present climatologies (Remer and Kaufman 1998; Remer et al. 1998), is used to retrieve aerosol properties over land from spaceborne MODIS measurements (Kaufman et al. 1997a). New techniques have recently been developed to derive the single scattering albedo and refractive indices of the total aero-

sol column under ambient conditions from ground-based and satellite remote sensing (Yamasoe et al. 1998; Martins et al. 1998; Dubovik et al. 1998). Following careful evaluation of the accuracy of these retrievals, they could potentially replace the present climatology of these parameters.

4. Satellite sensors

Remote sensing of aerosol optical properties from space has, in the past, been accomplished using satellite data not explicitly designed with this application in mind. This has included AVHRR data, whose primary purpose has been the determination of sea surface temperature and vegetation index, and TOMS data, whose primary purpose has been the derivation of total ozone content. Table 1 shows a timeline of satellite-based tropospheric aerosol optical thickness observations from 1981 to 2005. A summary of some of the salient features of these sensor systems is outlined below.

a. Past (1981–98)

The most frequently used satellite sensor for aerosol optical thickness retrievals is AVHRR, a five-band cross-track scanning radiometer flown on NOAA polar orbiting satellites since 1978. Since this sensor has no onboard calibration of the visible bands, those most important for aerosol retrievals over the ocean, extensive effort has been required to assess and monitor the calibration of each individual sensor in this overlapping time series. NOAA has routinely retrieved aerosol optical thickness over the ocean since 1981 using the afternoon polar orbiting satellites only (*NOAA-7, -9, -11, -14*), where their single-band algorithm was applied only to the backscattering half of the scan swath in order to avoid sun glint. In spite of these shortcomings, most of what we know about aerosol properties over the ocean (Husar et al. 1997) has been derived from this sensor using a single wavelength algorithm (Rao et al. 1989; Stowe et al. 1997).

The other long-term sensor used recently for aerosol characterization is TOMS, initially launched in 1978 on *Nimbus-7* and extensively used for total ozone content derivation. This ultraviolet scanning monochromator has a large field of view (50 km). It is especially sensitive to absorbing aerosol particles, both over land and ocean, but is hampered in doing quantitative aerosol analysis by its large footprint, which makes subpixel cloud contamination by far its largest problem, and uncertainties in the height of the aerosol layer (Torres et al. 1998).

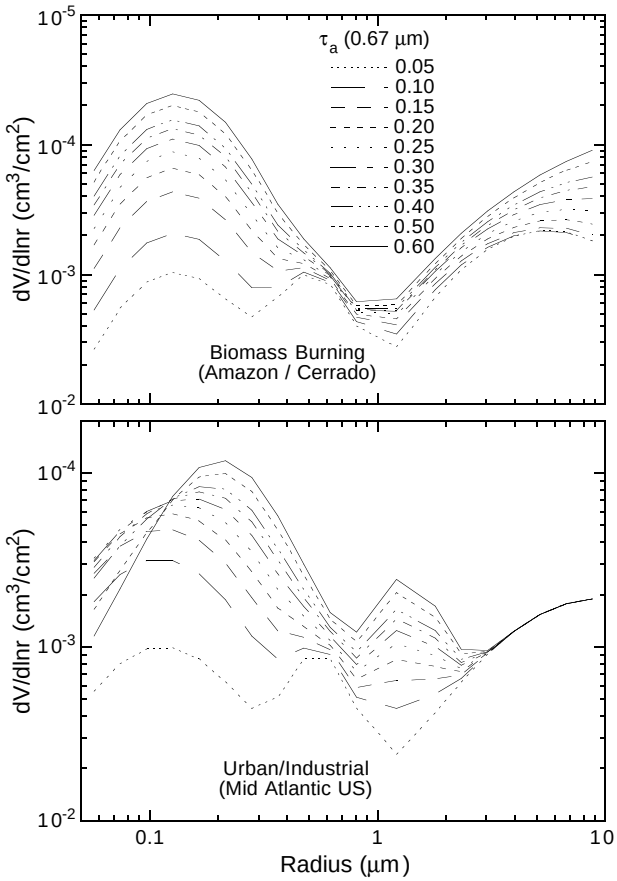

FIG. 6. Aerosol models derived from AERONET measurements in the Amazon for smoke aerosol (top) and mid-Atlantic industrial/urban aerosol (bottom). Four main modes of aerosol can be distinguished: (i) accumulation mode ($r < 0.3$ μm) of mostly organic smoke particles or sulfates in the urban/industrial aerosol, (ii) largely aerosol-free troposphere plus stratospheric aerosol (0.3 μm $< r < 0.8$ μm), (iii) maritime salt particles in the mid-Atlantic region (0.8 μm $< r < 2.5$ μm), and (iv) coarse particles ($r > 2.5$ μm) (adapted from Remer et al. 1996).

In 1995 ESA launched a new type of multiangle sensor, again for the purpose of improving the accuracy of sea surface temperature determination rather than for aerosol retrievals per se. This conically scanning sensor, ATSR-2, was launched on *ERS-2* in April 1995. With a time difference of 2 min between its forward scan and its near-nadir scan, aerosol retrievals can in principle be achieved (Veefkind et al. 1998, 1999). This sensor has yet to be applied to global retrievals of aerosol optical properties but, given the similarity of its bands to those of AVHRR and with its two different look angles, the potential for improved aerosol retrievals from this sensor exists.

TABLE 1. Time line of instruments and spacecraft used to derive aerosol properties from space.

Instrument	Spacecraft	1980				1985				1990				1995				2000				2005
AVHRR	*NOAA-7*, *-9*, *-11*, *-14*, -L, Metop-1		■	■	■	■	■	■	■	■	■	■	■	■	■	■	■	■	■	■	■	■
TOMS	*Nimbus-7*, Meteor, EP, ADEOS, QuikTOMS		■	■	■	■	■	■	■	■	■	■	■	■	■	■	■	■	■	■	■	
ATSR-2	*ERS-2*													■	■	■	■	■				
OCTS	ADEOS														■	■						
POLDER	ADEOS, ADEOS II														■	■			■	■	■	■
SeaWiFS	*OrbView-2*															■	■	■	■			
MISR	Terra																	■	■	■	■	■
MODIS	Terra, EOS PM																	■	■	■	■	■
AATSR	Envisat-1																		■	■	■	■
MERIS	Envisat-1																		■	■	■	■
GLI	ADEOS II																		■	■	■	■
OMI	EOS CHEM																			■	■	■

The Japanese launched the first of their ADEOS satellites in 1996. It contained both POLDER, a polarization-sensitive charge-coupled device (CCD) camera from the Centre National d'Etudes Spatiales (CNES), the French Space Agency, and OCTS, provided by NASDA. POLDER is the first space sensor designed with aerosol retrievals in mind, and this sensor has been used both for aerosol retrievals over ocean and over land, where the polarized radiance alone has been used to derive aerosol properties over land. OCTS was designed primarily for ocean color and sea surface temperature purposes, but has been successfully applied to aerosol retrievals over the ocean. Neither of these sensors had onboard calibration for the shortwave channels, and thus relied on preflight calibration as well as postflight vicarious calibration using ground-based measurements. Due to a failure in the solar panel assembly on the ADEOS spacecraft, this mission was limited to only 8 months of data acquisition.

In 1997 NASA and OrbImage launched the SeaWiFS sensor, a commercial partnership aimed at obtaining ocean color data globally for use by fisherman worldwide. This very capable sensor, which, like OCTS, has the ability to tilt to avoid sun glint in the Tropics, has been used to retrieve aerosol optical thickness over the ocean. Since it has no thermal bands and no onboard calibrators, its primary drawbacks are its limited spectral range making cloud screening especially difficult, and the need to do careful postlaunch calibration monitoring using solar and lunar views of the sensor.

Table 2 summarizes the primary sensors that have been used for the derivation of aerosol optical properties from space, and describes a number of key distinguishing features of each instrument, including swath width, pixel size, sensor characteristics, and advantages and limitations. Figure 7 illustrates the spectral transmission of the atmosphere from 0.3 to 20 μm, based on MODTRAN calculations for a midlatitude summer atmosphere when the sun is overhead and the spacecraft is viewing toward nadir. Superimposed on this figure are the locations and bandwidths of all channels of the 12 instruments discussed in this paper, where we have indicated what bands are used for aerosol retrievals over ocean and land, and what bands are used for cloud mask determination. It is clear from this figure that early sensors like AVHRR had broad bands for enhanced signal to noise, whereas TOMS used a combination of narrow bandwidth and large footprint to accomplish high signal-to-noise levels.

b. Future (1999–2005)

A major improvement in tropospheric aerosol remote sensing capabilities will continue with the launch of the NASA Terra satellite in 1999. This spacecraft carries two sensors specifically designed with aerosol remote sensing in mind, MODIS and MISR. MODIS

is a 36-band spectroradiometer with moderate spatial resolution (250–1000 m) and sophisticated onboard calibrators. The aerosol retrieval algorithms use six bands over ocean and six bands over land (cf. Fig. 7). A particular strength of MODIS over its predecessors is the availability of 17 bands for discriminating clouds, shadows, heavy aerosol, and fires (Ackerman et al. 1998; King et al. 1998). This sensitivity includes the ability to detect cirrus clouds using both the CO_2 slicing channels and the 1.38-μm channel, as well as improved resolution of boundary layer cellular cloud fields (250 m–1 km spatial resolution). MISR, on board the same spacecraft, will use nine CCD-based pushbroom cameras to view multiple angles (four forward, four backward, and nadir) at four wavelengths. Through the use of multiple wavelengths and multiple view angles, MISR should be able to retrieve aerosol optical thickness and aerosol type over both land and ocean. With the focal length of its nine cameras, it has a swath width of 360 km and thus requires 9 days to cover the globe.

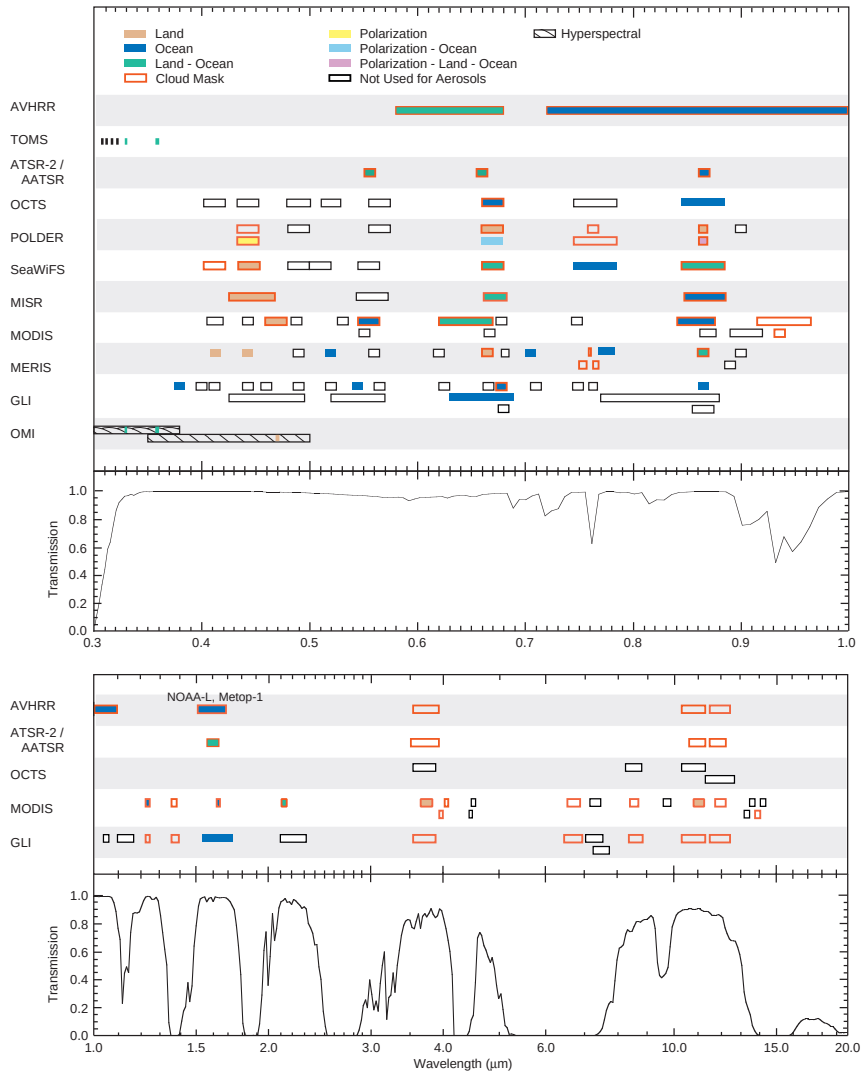

FIG. 7. Spectral transmission of the midlatitude summer atmosphere as a function of wavelength from 0.3 to 20 μm. Computations were performed using MODTRAN for overhead sun and nadir observations from space. The location and bandwidths of 12 satellite sensors are also shown in the figure. We have identified the purpose to which the bands are applied for aerosol retrieval over the ocean, land, or both, and what bands are used for cloud screening.

Envisat-1 is ESA's advanced environmental satellite and is scheduled for launch in 2000. It will carry an AATSR, identical to ATSR-2 (described above) except for procedures used to calibrate the sensors, and MERIS (Medium Resolution Imaging Spectrometer). MERIS will make use of daytime cloud heights derived using the oxygen A-band in order to screen for cloud-free pixels. It has no thermal infrared capability for determining a cloud mask and, hence, will have to rely on the oxygen A-band absorption characteristics, together with radiance threshold techniques.

NASDA is planning to launch the ADEOS II satellite in 2000. This spacecraft carries, in addition to POLDER, the GLI (Nakajima et al. 1998), a 36-band spectroradiometer in many ways similar to MODIS. It contains six 250-m bands, but is unable to record them globally due to data rate limitations on board the spacecraft. GLI will have considerable capability to do aerosol retrievals over ocean and land and will make use of a very similar cloud mask to that developed for MODIS. It lacks the CO_2 slicing bands of MODIS (cloud-top altitude bands) but has oxygen A-band and ultraviolet bands that will make cloud screening and aerosol retrievals robust.

The Netherlands Agency for Aerospace Programs is planning to provide the Ozone Monitoring Instru-

TABLE 2. Instruments, spacecraft, and principal characteristics of sensors used for the remote sensing of aerosol properties from space.

Instrument	Spacecraft	Spatial resolution (km)	Swath width (km)	Sensor characteristics	Comments
AVHRR	*NOAA-7*, *-9*, *-11*, *-14*, -L, Metop-1	1.1 (local mode); 4.4 (global)	2800	Cross-track scanner with five spectral bands	Relatively long-term dataset (since 1979); limited calibration accuracy (no internal calibration); near-infrared band influenced by water vapor absorption
TOMS	*Nimbus-7*, *Meteor-3*, ADEOS, Earth Probe, QuikTOMS	50	3000	Fixed-grating monochromator resolves incoming light into six bands	Relatively long-term dataset (since 1978); sensitive to absorbing aerosols over land and ocean; lower spatial resolution than comparable imaging radiometers
ATSR-2	*ERS-2*	1	500	Conical scanner with two views of the earth (forward look angle of 55°, and near nadir), separated in time by 2 min; seven spectral bands	Multi-look-angle sensor not specifically designed for aerosol retrievals; narrow swath width, taking 6 days for global coverage
OCTS	ADEOS	0.7	1400	Cross-track scanning radiometer with 12 spectral bands; tilt capability (±20°) to avoid sun glint	Has three thermal channels that can be used for cloud screening; no onboard calibrators; requires resampling for registration of bands
POLDER	ADEOS, ADEOS II	7×6	2200	Bidimensional CCD matrix and rotating wheel that carries filters and polarizers with a large field-of-view (114°) lens	Polarization more sensitive to aerosol refractive index than radiance; observes earth targets from 12 directions; uses A-band, reflectance thresholds, and spatial coherence for cloud screening; no onboard calibrators
SeaWiFS	OrbView-2	1.1 (local mode); 4.5 (global)	2800	Cross-track scanning radiometer with eight spectral bands; tilt capability (±20°) to avoid sun glint	Has no thermal channels for cloud screening; solar and lunar maneuvers for calibration

ment (OMI) for NASA's EOS CHEM satellite in 2002. This instrument is a 740-band hyperspectral imaging grating spectrometer in pushbroom mode, with spectral bands extending from 270 to 500 nm. Each pixel in its 2600-km-wide swath has an instantaneous field of view of 3 km, binned to 13 km × 24 km for global mode and, on occasion, to 13 km × 13 km in local mode for the purpose of detecting and tracking urban-scale pollution sources. OMI will have considerable capability to do aerosol retrievals over ocean and land following the approach adopted by TOMS, but at much enhanced spatial resolution.

Table 3 summarizes the principal techniques that have or will be applied to the remote sensing of global

TABLE 2. *Continued*.

Instrument	Spacecraft	Spatial resolution (km)	Swath width (km)	Sensor characteristics	Comments
MISR	Terra	1.1	360	Nine CCD-based pushbroom cameras viewing nadir and fore and aft up to 70.5°; four visible and near-infrared bands	Has no thermal channels for cloud screening; uses high quantum efficiency diodes for in-flight calibration; takes 9 days for global coverage
MODIS	Terra, EOS PM	0.25–1	2330	Cross-track scanning spectroradiometer with 36 spectral bands	High calibration accuracy with many onboard calibrators and wide spectral range; ability to detect clouds, shadows, and heavy aerosol
AATSR	Envisat-1	1	500	Conical scanner with two views of the earth (forward look angle of 55°, and near nadir), separated in time by 2 min; seven spectral bands	Multi-look-angle sensor not specifically designed for aerosol retrievals; no onboard calibrators
MERIS	Envisat-1	0.3–1.2	1150	Cross-track scanner with tilt capability; 15 bands acquired and transmitted in flight	Oxygen A-band capability for cloud top altitude determination; no SWIR or thermal bands
GLI	ADEOS II	0.25–1	1600	Cross-track scanning spectroradiometer with 36 spectral bands	Wide spectral coverage with many bands at 250 m (locally available); ability to detect clouds, shadows, and heavy aerosol; inclusion of absorbing aerosol bands in the UV
OMI	EOS CHEM	13 (local mode); 13 × 24 (global)	2600	Wide field telescope feeding two hyperspectral pushbroom grating spectrometers with 740 spectral bands from 270 to 500 nm	High calibration accuracy with many onboard calibrators; no thermal channels for cloud screening

aerosol properties from space, identifying both the major approaches that are applicable to a particular sensor and the principal assumptions behind each technique.

5. Aerosol retrievals from existing satellite systems

The most frequently used satellite sensor for deriving aerosol optical thickness over the ocean is NOAA's AVHRR. Figure 8a shows the aerosol optical thickness at 0.63 μm (channel 1) retrieved for the month of April 1997. High aerosol concentrations in the Northern Hemisphere—especially off the east coast of the United States, China, and the Indian Ocean—large aerosol plumes off the Sahelian region of northern Africa, and low concentrations of aerosol in the Southern Hemisphere, are all quite apparent.

The TOMS inversion procedure uses the ratio of the reflectances R_{340}/R_{380} and the R_{380} reflectance to form calculated tables of aerosol optical thickness and single scattering albedo (Torres et al. 1998), as de-

TABLE 3. Techniques for remote sensing of global aerosol properties from space. Here, τ_a denotes aerosol optical thickness, ω_0 the single scattering albedo, r_e the aerosol particle effective radius, and $n_c(r)$ the columnar aerosol size distribution.

Technique	Aerosol property	Relevant satellite sensors	Principal assumptions	References
Ocean				
reflectance–one channel	τ_a	AVHRR	Size distribution, ocean reflectance, whitecaps, calibration, ω_0	Griggs (1975); Mekler et al. (1977); Quenzel and Koepke (1984); Fraser et al. (1984); Stowe et al. (1997)
reflectance–multiple channels	τ_a, $n_c(r)$	GLI, MERIS, MISR, MODIS, OCTS, POLDER, SeaWiFS, AVHRR, TOMS, OMI	Type of size distribution, ocean reflectance, whitecaps, calibration, ω_0	Durkee et al. (1986, 1991); Tanré et al. (1997); J. R. Herman et al. (1997); Fukushima and Toratani (1997); Higurashi and Nakajima (1999)
Land				
reflectance	τ_a	AVHRR, TOMS, OMI	Size distribution, no change in surface reflectance, ω_0 (to derive τ_a)	Fraser et al. (1984); Kaufman et al. (1990a,b); Fraser (1993)
reduction in contrast	τ_a	AVHRR, GLI, MODIS, POLDER	No change in surface reflectance, bidirectional reflectance, ω_0, asymmetry factor	Tanré et al. (1988b); Tanré and Legrand (1991); Holben et al. (1992)
dark targets over dense dark vegetation	τ_a	AVHRR, GLI, MERIS, MISR, MODIS, POLDER, SeaWiFS	Reflectance of dark targets, size distribution, ω_0	Kaufman and Sendra (1988); King et al. (1992); Kaufman et al. (1997a,b)
thermal contrast	τ_a	AVHRR, GLI, MODIS		Legrand et al. (1989); Tanré and Legrand (1991); Ackerman (1997);
Land–ocean contrast	τ_a, ω_0, r_e	AVHRR, GLI, MODIS, POLDER	Size distribution and surface bidirectional reflectance	Kaufman and Joseph (1982); Fraser and Kaufman (1985); Kaufman et al. (1990a); Nakajima and Higurashi (1997)
Angular distribution of reflectance	τ_a, $n_c(r)$	ATSR-2, AATSR, MISR, POLDER	Surface bidirectional reflectance	Martonchik and Diner (1992); Wang and Gordon (1994); Veefkind and de Leeuw (1997)
Polarization	τ_a, $n_c(r)$	POLDER	Reflectance and polarization of underlying surface, spherical particles	Leroy et al. (1997); Mishchenko and Travis (1997); M. Herman et al. (1997)

scribed in Eq. (9). Figure 8b shows the optical thickness at 0.380 μm derived from TOMS data for April 1997, assuming the aerosol layer was at 3 km and the ultraviolet surface reflectivity was based on the climatology developed by Herman and Celarier (1997). As discussed by Torres et al., the derived optical thickness is sensitive to aerosol layer height only when aerosols are highly absorbing, but not otherwise. Uncertainty due to surface reflectivity is about 0.1 in optical thickness. Cloud contamination effects were reduced by setting an upper limit on the R_{380} reflectance. In comparison to Fig. 8a, the aerosol optical thickness from TOMS (Fig. 8b) shows larger optical thickness due to the shorter wavelength, as expected (note different color scale in Fig. 8b). In addition to the high aerosol optical thickness regions evident in Fig. 8a, the TOMS aerosol retrieval includes aerosol optical thickness over the land, and shows quite clearly the large optical thickness in the wind-blown dust regions of Sahelian Africa, the Arabian Peninsula, Amazonas, Brazil, and Southeast Asia.

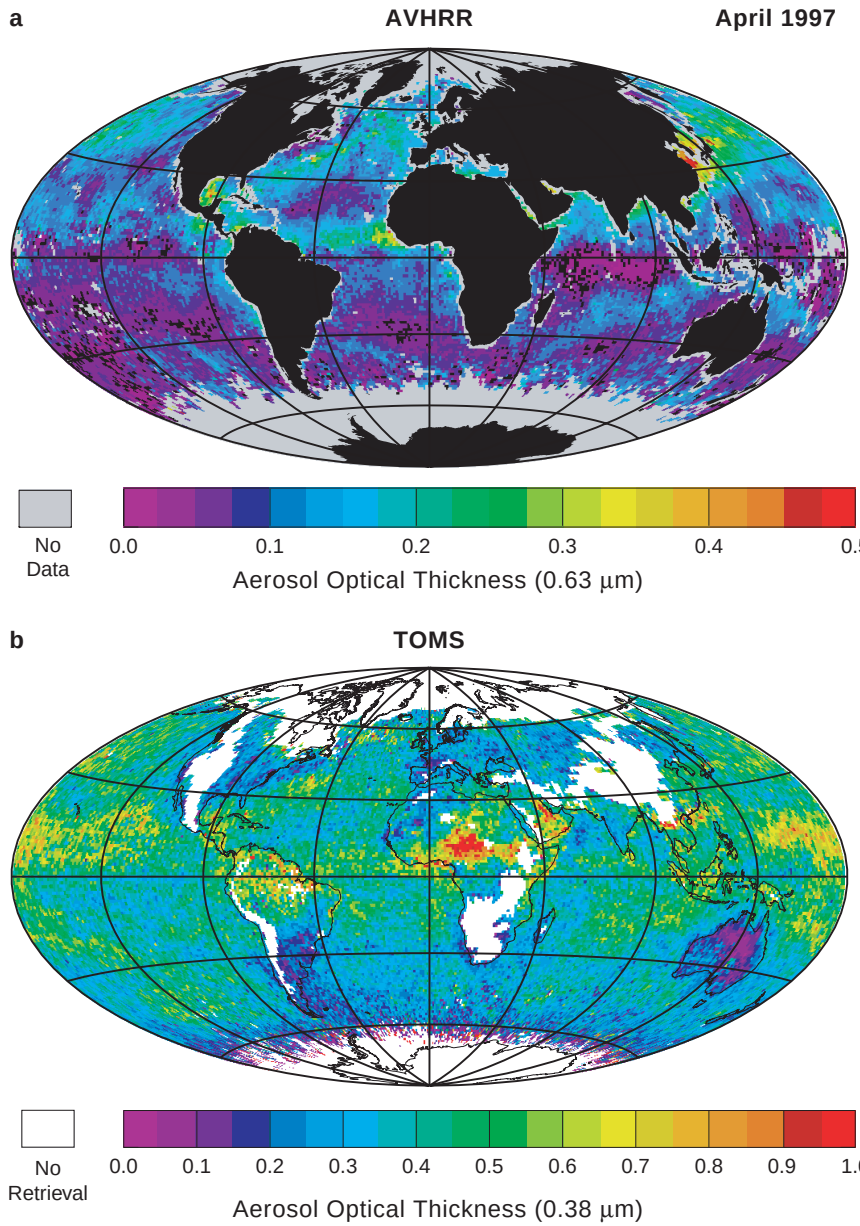

FIG. 8. (a) Aerosol optical thickness (0.63 μm) from AVHRR data and (b) TOMS data (0.38 μm) in Apr 1997.

The use of polarization for the remote sensing of aerosol from space is demonstrated in Fig. 9, which shows a POLDER image acquired over France on 10 March 1997. The left-hand image is a red (0.865 μm), green (0.670 μm), blue (0.443 μm) composite of the total radiance, and the right-hand image the corresponding red–green–blue (RGB) composite of polarized radiance (Stokes vector Q). As expected (Deuzé et al. 1993; M. Herman et al. 1997), the polarized radiance resulting from the reflection of light from the surface is small compared with the polarized radiance due to aerosol and molecular scattering. As a result, the boundaries of the continents largely disappear and the polarized signal can thus be related to the scattering properties of the atmosphere. Only in the case of sun glint to the west of Corsica and Sardinia does the polarized radiation exhibit strong features of the underlying surface. Quantitative analysis of images such as these requires a correction for molecular scattering, which affects the outgoing radiance and polarization, primarily in the blue. Nonvegetated surfaces such as bare soils in desert regions contribute to a larger extent to the satellite signal than do vegetated surfaces, but the concept is valid over most land surfaces. For low aerosol content, correction of the surface contribution must be applied, but

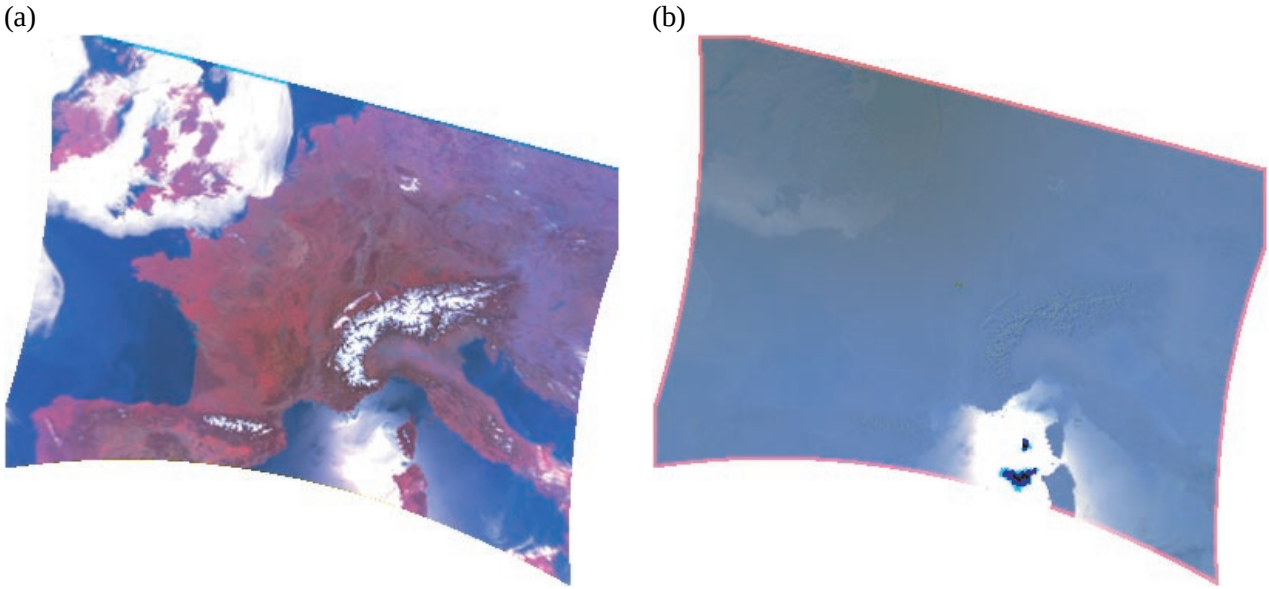

FIG. 9. First false-color images (10 Mar 1997) acquired by the POLDER instrument aboard the Japanese ADEOS platform (CNES/NASDA), where (a) is the total radiance and (b) is the polarized radiance. Both images were formed from red–green–blue composites of the 865-, 670-, and 443-nm channels.

it is easier than for the total radiance since surface polarization features are more uniform and constant over time (Nadal and Bréon 1999).

Characterization of aerosol optical properties over the ocean is improved with POLDER through the use of spectral information for deriving aerosol size distribution in addition to the angular ability to avoid sun glint. The determination of the Ångström exponent (from the 0.670- and 0.865-μm channels) allows a better estimate of the aerosol optical thickness through a better estimation of the aerosol phase function (Deuzé et al. 1999). The resulting optical thickness accuracy has been estimated to be of the order $\Delta\tau_a \sim 0.05$, whereas comparisons of the retrieved Ångström exponent with ground-based measurements indicate a systematic underestimate of the order of 30% from POLDER (Goloub et al. 1999). This underestimate has not yet been explained and, for the moment, there is no strong evidence of any possible physical processes that are missing from the analysis and which would improve the relationship. The optical thickness at 0.865 μm and the Ångström exponent averaged for the month of April 1997 are shown in Fig. 10 (adapted from Deuzé et al. 1999). The Ångström exponent (Fig. 10b) is derived only when the aerosol optical thickness is larger than 0.1. For small aerosol content ($\tau_a < 0.1$), its value is prescribed ($\alpha = 0.0$) for matching a maritime aerosol model expected in these conditions. These results confirm that the Ångström exponent can be derived from space and used to discriminate aerosol type; large dust particles corresponding to small values of α off the west coast of Africa and biomass burning aerosols associated with large values of α, off the coast of central America, can clearly be identified.

Figure 11 shows a corresponding composite of retrieved aerosol optical thickness (at 0.5 μm) and Ångström exponent α derived from global OCTS data for April 1997 (adapted from Nakajima and Higurashi 1998). Again we have restricted our Ångström exponent analysis to $\tau_a(0.5\ \mu\text{m}) > 0.1$. Both OCTS and POLDER show similar features for optical thickness and Ångström exponent. These features include (i) dust transport over the tropical Atlantic Ocean between the Sahel and the Lesser Antilles, (ii) biomass burning aerosols in Central America, and (iii) small sulfate particles off the east coast of the United States, western Europe, and Asia. All of these regions are characterized by having small particles, and the Ångström exponent is more sensitive to aerosol characteristics than optical thickness. Large aerosol particles (low α) with low optical thickness were the dominant feature over most of the world's oceans. Nevertheless, the retrieved values of optical thickness and Ångström exponent tend to be larger for OCTS than from POLDER for both aerosol parameters.

There are several possible explanations for these differences, among which are (i) wavelength—OCTS

uses a smaller wavelength (0.5 μm) than POLDER (0.865 μm), which results in larger values of optical thickness for OCTS but no difference in Ångström exponent; (ii) calibration of the sensors (Hagolle et al. 1999), where calibration errors result in biases in derived aerosol optical thickness (cf. Fig. 2); and (iii) cloud mask (Bréon and Colzy 1999), where undetected subpixel clouds result in an overestimation of aerosol optical thickness and an underestimation of Ångström exponent. For the OCTS aerosol retrievals presented in Fig. 11, thermal infrared channels were not yet available for use in cloud detection. This shortcoming led in turn to some cloud contamination in the aerosol retrievals, especially evident in retrievals over the Southern Ocean.

Figures 10 and 11 represent the first time that different instruments on the same spacecraft have been used to provide similar information on aerosol optical properties and composition, and both of these were analyzed over the ocean only. These preliminary results are quite encouraging and the above explanations will be further explored to more fully understand the origin of the present discrepancies that we have identified. Analyses such as these highlight the importance of a robust validation program to independently assess the accuracy, precision, and biases of satellite retrievals of aerosol optical properties. AERONET provides the best such global network for the evaluation of the accuracy of retrievals of aerosol optical thickness and size distribution parameters from spaceborne radiometers.

6. Future capabilities

The MODIS ocean algorithm was tested using MAS data acquired from the NASA ER-2 during the Tropospheric Aerosol Radiative Forcing Observational Experiment (TARFOX) (Tanré et al. 1999). The TARFOX campaign (Russell et al. 1999a) was conducted from 10 to 31 July 1996 off the mid-Atlantic coast of the United States and was designed to reduce uncertainties in aerosol radiative effects. The NASA ER-2 flew several times during the experiment above the University of Washington's C-131A research aircraft on which the six-channel Ames Airborne Tracking Sunphotometer (AATS-6) was mounted (Russell et al. 1999b). The retrieved aerosol properties could thus be tested against column aerosol optical thickness values derived from a low-flying in situ aircraft. The MAS optical thickness derived at 0.550 μm and its spectral dependence computed from the retrieved aerosol model is compared with the AATS-6 measurements in Fig. 12 for 25 July 1996.

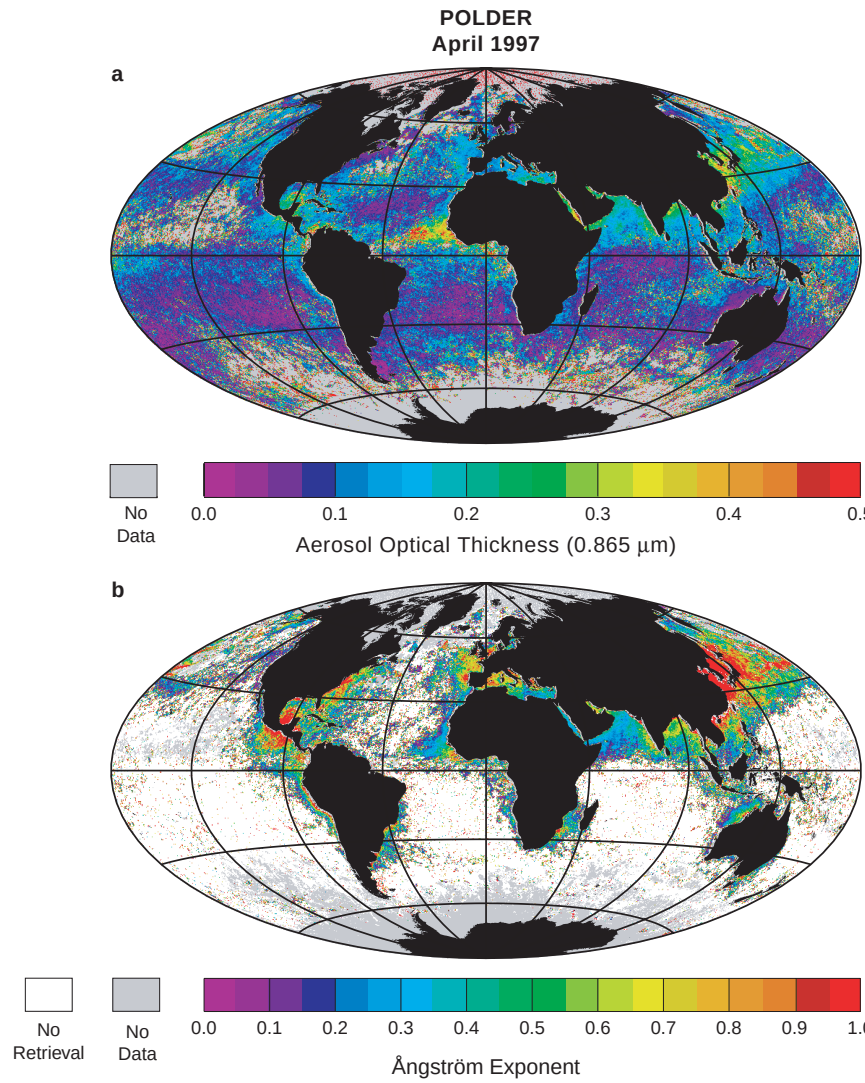

FIG. 10. (a) Aerosol optical thickness (0.865 μm) and (b) Ångström exponent derived from POLDER data in Apr 1997 (adapted from Deuzé et al. 1999).

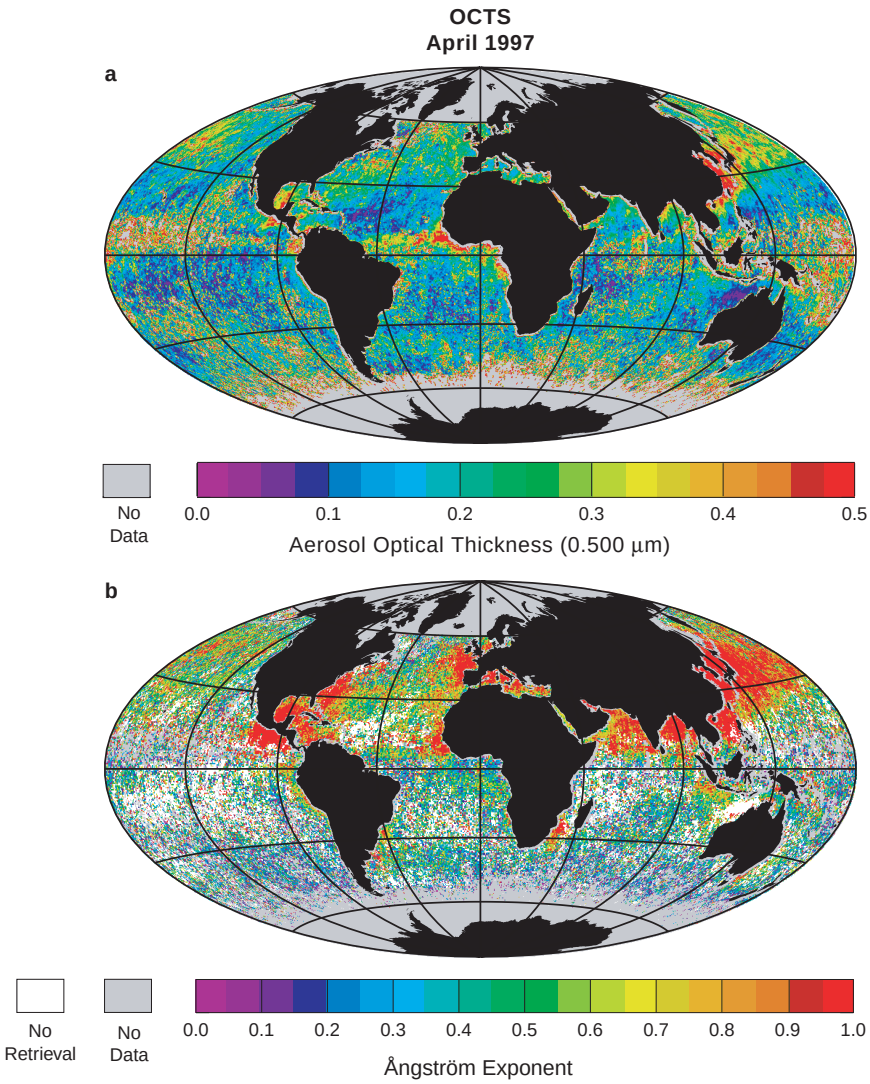

FIG. 11. As in Fig. 10 except for OCTS data at 0.500 μm (adapted from Nakajima and Higurashi 1998).

The agreement is very good (i.e., the optical thickness at 0.550 μm is very close to the sunphotometer value). Furthermore, the derived spectral dependence of optical thickness also matches the measurements quite well, which means that the aerosol model derived from the ER-2 remote sensing measurements uses the right optical properties.

The accuracy of the MODIS ocean and land algorithms are further demonstrated in Fig. 13, where the ocean algorithm is demonstrated on the left-hand side of the figure and the land algorithm on the right-hand side. In both cases, the data used to test these algorithms were MAS data of haze-filled boundary layers 150 km in length and 37 km in width, where the ER-2 was flying from top to bottom down the center of these images. For TARFOX, the MAS color composite image was constructed by contrast stretching and combining three spectral bands into RGB displays, where the RGB assignment was 0.66 μm (red), 0.55 μm (green), and 0.46 μm (blue). The aerosol optical thickness retrieved from these data using the MODIS ocean algorithm is illustrated to the right of the true-color composite image. Note the skillful avoidance of clouds in the analyzed field, which ran following the MAS cloud mask algorithm. A scatter diagram of all intercomparisons with the sunphotometer onboard the C-131A during TARFOX is shown under the color panels. The error bars in the figure correspond to spatial and temporal variation in aerosol optical thickness observed by the MAS-derived aerosol field and the sunphotometer, respectively.

The right-hand side of Fig. 13 shows an application of the algorithm developed for MODIS over land to data acquired from MAS aboard the NASA ER-2 aircraft during the Smoke, Clouds, and Radiation-Brazil (SCAR-B) experiment (Chu et al. 1998). The SCAR-B campaign was conducted from August to September 1995 in the Brazilian cerrado and rain forest regions, and was designed to monitor the radiative and microphysical properties of smoke arising from biomass burning. For SCAR-B, the MAS color composite image was constructed as an RGB image with assignments of 2.19 μm (red), 0.87 μm (green), and 0.65 μm (blue), which highlight the haze and smoke that appear blue, burn scars brown, unburned vegetation green, clouds white, and fires red. The aerosol optical thickness retrieved from these data using the MODIS land algorithm is illustrated to the right of this false-color image. Once again, these data yielded aerosol retrievals over most of this image, avoiding clouds, shadows on the ground, burn scars, and fire, as first identified by the MAS cloud mask applied to this scene (King et al. 1998).

During SCAR-B, most ER-2 flights included routine overpasses of ground-based AERONET sunphotometer sites (Kaufman et al. 1998b). A total of 20 overpasses of the ER-2 over six sunphotometer sites, including both rain forest and cerrado sites, were obtained with a good temporal match. Figure 13 shows a comparison between the aerosol optical thickness retrieved from MAS images and that obtained from coincident and concurrent ground-based sunphotometer measurements, both at 0.66 μm (see scatterplot beneath the color panels). These results, adapted from Chu et al. (1998), show excellent agreement over a wide dynamic range ($0.1 \le \tau_a \le 2.1$), with a slope of 0.97, an intercept of 0.03, and a correlation coefficient of 0.98. Note that all the retrieved aerosol optical thickness values fall within the anticipated range of retrieval errors (shown as the dotted–dashed lines) (Kaufman et al. 1997a). The vertical and horizontal error bars represent, respectively, the standard deviation of the spatial average of the MAS retrievals (typically within a $10 \times 10 - 25 \times 25$ km^2 area surrounding the sunphotometer sites) and the temporal average of the sunphotometer observations (±30 min of the ER-2 overpass time).

Although the present results need to be confirmed for other aerosol types (e.g., dust and smoke), the potential of MODIS data for retrieving aerosol parameters is clearly demonstrated. The error can be described by $\Delta\tau_a = 0.01 \pm 0.05\tau_a$ over the ocean for the aerosol type encountered during TARFOX; concerning the effective particle radius, comparisons confirm our previous accuracy estimate of $\Delta r_e = 0.3 r_e$ (Tanré et al. 1997). Over the land, the error can be described by $\Delta\tau_a = 0.05 \pm 0.15\tau_a$ for the aerosol type encountered in Brazil. In both cases the results are better than the theoretical predictions (Kaufman et al. 1997a; Tanré et al. 1997). The advanced capabilities demonstrated in Figs. 12 and 13 will routinely be applied to MODIS data to be acquired from the Terra satellite in 1999. These capabilities, together with the more advanced MODIS cloud mask (Ackerman et al. 1998), will permit enhanced capabilities that will lead to routine retrievals of aerosol optical thickness over land and ocean as well as aerosol size parameters over the ocean. Similar capabilities are possible with GLI, to be launched on ADEOS II in 2000, as well as MODIS on EOS PM.

Both MODIS and GLI have the unique ability to discriminate small low clouds using global observations at a few 250-m resolution bands. In addition, both sensors have the added feature of a narrow band at 1.375 μm, in a water vapor absorption band, that will be used to discriminate and correct for the effect of thin cirrus clouds on aerosol measurements (Gao and Kaufman 1995).

7. Conclusions

The recently rediscovered importance of tropospheric aerosol as a major source of uncertainty in the radiative forcing of climate and hence the prediction of climate change has fueled a resurgence of interest in the remote sensing of tropospheric aerosols from space. In the past we have primarily been restricted to using uncalibrated sensors that were not designed for the remote sensing of tropospheric aerosols, or to large field-of-view ultraviolet spectrometers that provide a useful aerosol index not easily converted to an aerosol optical thickness needed by climate models. Since 1996, however, with the launch of the ADEOS satellite with the POLDER and OCTS instruments on board, we entered a new era in the remote sensing of tropospheric aerosols from space. In the near future, with EOS, Envisat-1, and ADEOS II, we will have an unprecedented array of spaceborne sensors with unique characteristics that will enable quantitative aerosol observations on a global scale. These enhanced capabilities include much improved onboard calibration, use of deep space and lunar viewing for calibration and sensor degradation analysis, vigorous vicarious calibration using ground-based and airborne sensors, narrow spectral bands that avoid uncertain gaseous absorption, multispectral and multiangle ob-

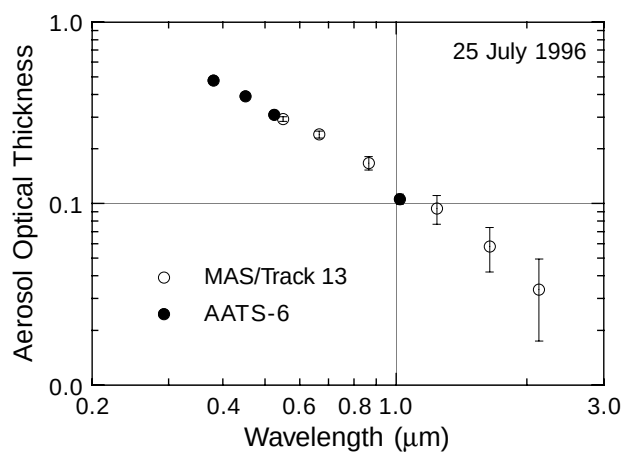

FIG. 12. Aerosol optical thickness measured by the sunphotometer (AATS-6) aboard the University of Washington C-131A aircraft and derived from MAS data as a function of wavelength during the TARFOX experiment on 25 Jul 1996 (adapted from Tanré et al. 1999).

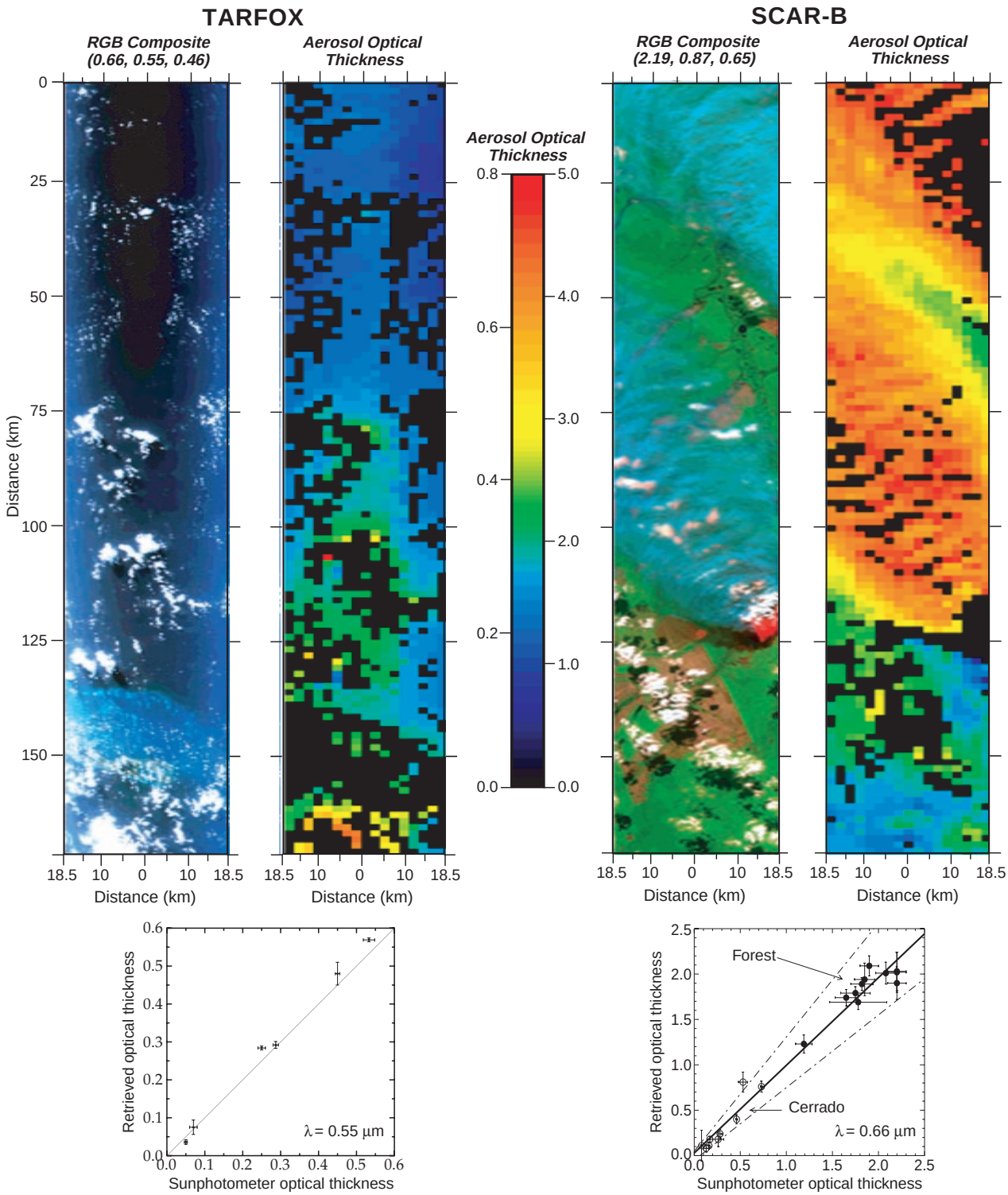

FIG. 13. MAS images and corresponding aerosol optical thickness retrievals for a 150 km × 37 km section of flight during TARFOX (ocean scene) and SCAR-B (land scene). The bottom two panels are the validation of the retrieved aerosol optical thickness in comparison to sunphotometer observations at 0.55 μm (TARFOX; University of Washington C-131A measurements) and 0.66 μm (SCAR-B; ground-based AERONET measurements).

servations, and polarization. These spaceborne instruments, when coupled with the AERONET network of sun/sky radiometers for the validation of the satellite data, derivation of aerosol models, and statistical characterization of aerosol in remote pristine environments, should make possible a much improved analysis of aerosol forcing of the earth–atmosphere–ocean system. These satellite and ground-based data, taken simultaneously with spaceborne observations of clouds, water vapor, trace gases, land cover, and the oceans, should enable an assessment of aerosol properties and their distribution in space and time, plus their interaction with clouds and the radiation field.

So far, analysis of satellite data on a global scale has been performed only for a single instrument at one time. Even the analysis of MODIS and MISR data will be performed separately, though they are both on the same spacecraft (Terra). With anticipated advancements in computer capability, as well as in our understanding of the remote sensing of aerosol properties from space, we anticipate that future algorithms will combine data from multiple instruments on a single platform, for example, MODIS and MISR on Terra, and on coordinated observations (e.g., EOS PM, PICASSO-CENA, and POLDER). Such algorithms can combine the use of angular measurements (MISR, POLDER) with information from a wide spectral range (MODIS), vertical distribution (PICASSO-CENA), polarization (POLDER), and precise cloud screening (MODIS, PICASSO-CENA).

Remote observations of aerosol, together with aerosol physical and optical properties, permit one to couple the spaceborne measurements with ground-based and airborne measurements of the size-dependent aerosol chemical composition and hence to describe the impact of aerosols on climate. But will we be able to use the satellite data to assess the global aerosol direct and indirect forcing of climate and reduce the uncertainty in predicting climate change? While spaceborne instruments have been designed to measure accurately the regional changes of aerosol loading for optical thicknesses $\tau_a > 0.1$, they are likely to do a relatively poor job in remote locations far from major sources, such as the central Pacific and southern Indian Oceans (cf. Figs. 8, 10, and 11). In regions such as these, the environment still contains small concentrations of aerosol that are widespread but still relevant to the global radiative forcing of the earth–atmosphere–ocean system by aerosols. Presently we do not know what fraction of the anthropogenic aerosol forcing comes from regions with optical thickness $\tau_a > 0.1$, values that are the most easily measured from space. Furthermore, the addition of active sensors (such as lidars) makes it possible to measure thin aerosol layers not easily observed using multispectral scanners. This is important because aerosol vertical distribution, critical to understanding aerosol interaction with clouds and with the radiation field around clouds, is impossible to infer any other way. Well-calibrated radiometers that, together with lidar measurements, observe the same spot from different directions and over a wide spectral range, can increase the accuracy of tropospheric aerosol measurements, especially for low optical thickness conditions. Polarization can further help in defining the aerosol refractive index. Finally, these measurements can be used to derive, on a statistical basis, the aerosol optical properties in remote regions. This is an exciting era of aerosol research, and we have tried to share this excitement with you in this paper.

Acknowledgments. The authors are grateful to Jason Li and Tom Arnold, SM&A Corp. (East), and Ward Meyer and Rong Rong Li, Science Systems and Applications Inc., for data processing and computer graphics support. We are especially grateful to Dr. Larry Stowe of NOAA/NESDIS as well as two anonymous referees for their very thoughtful and detailed reviews that contributed substantially to strengthening the paper. We would also like to thank Drs. Omar Torres (University of Maryland–Baltimore County), Jay Herman (Goddard Space Flight Center), Larry Stowe, and Allen Chu (Science Systems and Applications Inc.) for providing many of the satellite data and aircraft images used in this paper. This research was supported by the MODIS Science Team and the EOS Project Science Office.

Appendix: Acronyms

AATS	Ames Airborne Tracking Sunphotometer
AATSR	Advanced Along-Track Scanning Radiometer
ADEOS	Advanced Earth Observing Satellite
AERONET	Aerosol robotic network
ATSR	Along-Track Scanning Radiometer
AVHRR	Advanced Very High Resolution Radiometer
AVIRIS	Airborne Visible and Infrared Imaging Spectrometer
CCD	Charge-coupled device
CNES	Centre National d'Etudes Spatiales
CZCS	Coastal Zone Color Scanner
DDV	Dense Dark Vegetation
ECLATS	Etude de la Couche Limité Atmosphérique Tropical Sèche

EOS	Earth Observing System
EOSP	Earth Observing Scanning Polarimeter
ERS	Earth Remote Sensing satellite
ESA	European Space Agency
GLI	Global Imager
GOES	Geostationary Operational Environmental Satellite
LUT	Look-Up Table
MAS	MODIS Airborne Sensor
MERIS	Medium Resolution Imaging Spectroradiometer
MISR	Multi-angle Imaging Spectroradiometer
MODIS	Moderate Resolution Imaging Spectroradiometer
MSS	Multispectral Scanner
NASA	National Aeronautics and Space Administration
NASDA	National Space Development Agency (Japan)
NDVI	Normalized difference vegetation index
NOAA	National Oceanic and Atmospheric Administration
OCTS	Ocean Color and Temperature Scanner
OMI	Ozone Monitoring Instrument
PICASSO–CENA	Pathfinder Instruments for Cloud and Aerosol Spaceborne Observations–Climatologie Etendue des Nuages et des Aerosols
POLDER	Polarization and Directionality of the Earth's Reflectances
RGB	Red–green–blue
SAGE	Stratospheric Aerosol and Gas Experiment
SCAR-B	Smoke, Clouds, and Radiation-Brazil
SeaWiFS	Sea-viewing Wide Field-of-view Sensor
SWIR	Shortwave infrared
TARFOX	Tropospheric Aerosol Radiative Forcing Observational Experiment
TM	Thematic Mapper
TOMS	Total Ozone Mapping Spectrometer

References

Ackerman, S. A., 1989: Using the radiative temperature difference at 3.7 and 11 μm to track dust outbreaks. *Remote Sens. Environ.*, **27**, 129–133.

——, 1997: Remote sensing aerosols using satellite infrared observations. *J. Geophys. Res.*, **102**, 17 069–17 079.

——, K. I. Strabala, W. P. Menzel, R. A. Frey, C. C. Moeller, and L. E. Gumley, 1998: Discriminating clear-sky from clouds with MODIS. *J. Geophys. Res.*, **103**, 32 141–32 158.

Arnold, G. T., M. D. King, S. C. Tsay, J. Y. Li, and P. F. Soulen, 1999: Airborne spectral measurements of surface-atmosphere anisotropy for Arctic sea ice and tundra. *Int. J. Remote Sens.*, submitted.

Bouffiès, S., F. M. Bréon, D. Tanré, and P. Dubuisson, 1997: Atmospheric water vapor estimate by a differential absorption technique with the POLDER instrument. *J. Geophys. Res.*, **102**, 3831–3841.

Bréon, F. M., and S. Colzy, 1999: Cloud detection from the spaceborne POLDER instrument and validation against surface synoptic observations. *J. Appl. Meteor.*, **38,** 777–785.

Chandrasekhar, S., 1960: *Radiative Transfer.* Dover, 393 pp.

Charlson, R. J., S. E. Schwartz, J. M. Hales, R. D. Cess, J. A. Coakley Jr., J. E. Hansen, and D. J. Hofmann, 1992: Climate forcing by anthropogenic aerosols. *Science*, **255**, 423–430.

Christopher, S. A., D. V. Kliche, J. Chou, and R. M. Welch, 1996: First estimates of the radiative forcing of aerosols generated from biomass burning using satellite data. *J. Geophys. Res.*, **101**, 21 265–21 273.

Chu, D. A., Y. J. Kaufman, L. A. Remer, and B. N. Holben, 1998: Remote sensing of smoke from MODIS airborne simulator during the SCAR-B experiment. *J. Geophys. Res.*, **103**, 31 979–31 988.

d'Almeida, G. A., P. Koepke, and E. P. Shettle, 1991: *Atmospheric Aerosols, Global Climatology and Radiative Characteristics.* A. Deepak Publ., 561 pp.

Deschamps, P. Y., F. M. Bréon, M. Leroy, A. Podaire, A. Bricaud, J. C. Buriez, and G. Sèze, 1994: The POLDER mission: Instrument characteristics and scientific objectives. *IEEE Trans. Geosci. Remote Sens.*, **32**, 598–615.

Deuzé, J. L., F. M. Breon, P. Y. Deschamps, C. Devaux, M. Herman, A. Podaire, and J. L. Roujean, 1993: Analysis of the POLDER (Polarization and Directionality of Earth's Reflectances) airborne instrument observations over land surfaces. *Remote Sens. Environ.*, **45**, 137–154.

——, M. Herman, P. Goloub, D. Tanré, and A. Marchand, 1999: Characterization of aerosols over the ocean from POLDER. *Geophys. Res. Lett.*, **26**, 1421–1424.

Diner, D. J., and Coauthors, 1989: MISR: A Multiangle Imaging Spectro-Radiometer for geophysical and climatological research from EOS. *IEEE Trans. Geosci. Remote Sens.*, **27**, 200–214.

Dubovik, O., B. N. Holben, Y. J. Kaufman, M. Yamasoe, A. Smirnov, D. Tanré, and I. Slutsker, 1998: Single-scattering albedo of smoke retrieved from the sky radiance and solar transmittance measured from ground. *J. Geophys. Res.*, **103**, 31 903–31 924.

Durkee, P. A., D. R. Jensen, E. E. Hindman, and T. H. Vonder Haar, 1986: The relationship between marine aerosols and satellite detected radiance. *J. Geophys. Res.*, **91**, 4063–4072.

——, F. Pfeil, E. Frost, and R. Shema, 1991: Global analysis of aerosol particle characteristics. *Atmos. Environ.*, **25A**, 2457–2471.

Eck, T. F., B. N. Holben, I. Slutsker, and A. Setzer, 1998: Measurements of irradiance attenuation and calculation of aerosol single scattering albedo for biomass burning aerosols in Amazonia. *J. Geophys. Res.*, **103**, 31 865–31 878.

Ferrare, R. A., R. S. Fraser, and Y. J. Kaufman, 1990: Satellite remote sensing of large-scale air pollution: Measurements of forest fire smoke. *J. Geophys. Res.*, **95**, 9911–9925.

Fraser, R. S., 1976: Satellite measurement of mass of Sahara dust in the atmosphere. *Appl. Opt.*, **15**, 2471–2479.

——, 1993: Optical thickness of atmospheric dust over Tadjikistan. *Atmos. Environ.*, **27A**, 2533–2538.

——, and Y. J. Kaufman, 1985: The relative importance of aerosol scattering and absorption in remote sensing. *IEEE Trans. Geosci. Remote Sens.*, **23**, 625–633.

——, ——, and R. L. Mahoney, 1984: Satellite measurements of aerosol mass and transport. *Atmos. Environ.*, **18**, 2577–2584.

Fukushima, H., and M. Toratani, 1997: Asian dust aerosol: Optical effect on satellite ocean color signal and a scheme of its correction. *J. Geophys. Res.*, **102**, 17 119–17 130.

Gao, B. C., and Y. J. Kaufman, 1995: Selection of the 1.375-μm MODIS channel for remote sensing of cirrus clouds and stratospheric aerosols from space. *J. Atmos. Sci.*, **52**, 4231–4237.

Gathman, S. G., and K. L. Davidson, 1993: The Navy Oceanic Vertical Aerosol Model. NRaD Tech. Rep. 1634, NRAD, San Diego, CA, 111 pp. [NTIS No. AD-A278233/2INZ.]

Goloub, P., D. Tanré, J. L. Deuzé, M. Herman, A. Marchand, and F. M. Bréon, 1999: Validation of the first algorithm applied for deriving the aerosol properties over the ocean using the POLDER/ADEOS measurements. *IEEE Trans. Geosci. Remote Sens.*, **37**, 1586–1596.

Gordon, H. R., and M. Wang, 1994: Retrieval of water-leaving radiance and aerosol optical thickness over the oceans with SeaWiFS: A preliminary algorithm. *Appl. Opt.*, **33**, 443–452.

Griggs, M., 1975: Measurement of atmospheric aerosol optical thickness over water using ERTS-1 data. *J. Air Pollut. Contr. Assoc.*, **25**, 622–626.

Hagolle, O., and Coauthors, 1999: Results of POLDER in-flight calibration. *IEEE Trans. Geosci. Remote Sens.*, **37**, 1550–1566.

Herman, J. R., and E. Celarier, 1997: Earth's surface reflectivity climatology at 340-380 nm from TOMS data. *J. Geophys. Res.*, **102**, 28 003–28 012.

——, P. K. Bhartia, O. Torres, C. Hsu, C. Seftor, and E. Celarier, 1997: Global distributions of UV-absorbing aerosols from Nimbus 7/TOMS data. *J. Geophys. Res.*, **102**, 16 911–16 922.

Herman, M., J. L. Deuzé, C. Devaux, P. Goloub, F. M. Bréon, and D. Tanré, 1997: Remote sensing of aerosols over land surfaces including polarization measurements and application to POLDER measurements. *J. Geophys. Res.*, **102**, 17 039–17 049.

Higurashi, A., and T. Nakajima, 1999: Development of a two-channel aerosol retrieval algorithm on global scale using NOAA AVHRR. *J. Atmos. Sci.*, **56**, 924–941.

Hobbs, P. V., J. S. Reid, R. A. Kotchenruther, R. J. Ferek, and R. Weiss, 1997: Direct radiative forcing by smoke from biomass burning. *Science*, **275**, 1776–1778.

Holben, B. N., E. Vermote, Y. J. Kaufman, D. Tanré, and V. Kalb, 1992: Aerosol retrieval over land from AVHRR data—Application for atmospheric correction. *IEEE Trans. Geosci. Remote Sens.*, **30**, 212–222.

——, A. Setzer, T. F. Eck, A. Pereira, and I. Slutsker, 1996: Effect of dry season biomass burning on Amazon basin aerosol concentrations and optical properties, 1992–1994. *J. Geophys. Res.*, **101**, 19 465–19 481.

——, and Coauthors, 1998: AERONET—A federated instrument network and data archive for aerosol characterization. *Remote Sens. Environ.*, **66**, 1–16.

Hoppel, W. A., J. W. Fitzgerald, G. M. Frick, R. E. Larson, and E. J. Mack, 1990: Aerosol size distribution and optical properties found in the marine boundary layer over the Atlantic Ocean. *J. Geophys. Res.*, **95**, 3659–3686.

Houghton, J. T., L. G. Meira Filho, B. A. Callander, N. Harris, A. Kattenberg, and K. Maskell, Eds., 1996: *Climate Change 1995: The Science of Climate Change.* Intergovernmental Panel on Climate Change, Cambridge University Press, 572 pp.

Husar, R. B., J. M. Prospero, and L. L. Stowe, 1997: Characterization of tropospheric aerosols over the oceans with the NOAA Advanced Very High Resolution Radiometer optical thickness operational product. *J. Geophys. Res.*, **102**, 16 889–16 909.

Ignatov, A., L. Stowe, and R. Singh, 1998: Sensitivity study of the Angstrom exponent derived from AVHRR over the oceans. *Adv. Space Res.*, **21**, 439–442.

Kahn, R., R. West, D. McDonald, B. Rheingans, and M. I. Mishchenko, 1997: Sensitivity of multiangle remote sensing observations to aerosol sphericity. *J. Geophys. Res.*, **102**, 16 861–16 870.

Kattawar, G. W., 1975: A three-parameter analytic phase function for multiple scattering calculations. *J. Quant. Spectrosc. Radiat. Transfer*, **15**, 839–849.

Kaufman, Y. J., 1987: Satellite sensing of aerosol absorption. *J. Geophys. Res.*, **92**, 4307–4317.

——, 1993: Measurements of the aerosol optical thickness and the path radiance—Implications on aerosol remote sensing and atmospheric corrections. *J. Geophys. Res.*, **98**, 2677–2692.

——, and J. H. Joseph, 1982: Determination of surface albedos and aerosol extinction characteristics from satellite imagery. *J. Geophys. Res.*, **87**, 1287–1299.

——, and C. Sendra, 1988: Algorithm for automatic atmospheric corrections to visible and near-IR satellite imagery. *Int. J. Remote Sens.*, **9**, 1357–1381.

——, and B. C. Gao, 1992: Remote sensing of water vapor in the near IR from EOS/MODIS. *IEEE Trans. Geosci. Remote Sens.*, **30**, 871–884.

——, and L. A. Remer, 1994: Remote sensing of vegetation in the mid-IR: The 3.75 μm channels. *IEEE Trans. Geosci. Remote Sens.*, **32**, 672–683.

——, R. S. Fraser, and R. A. Ferrare, 1990a: Satellite remote sensing of large-scale air pollution: Method. *J. Geophys. Res.*, **95**, 9895–9909.

——, C. J. Tucker, and I. Fung, 1990b: Remote sensing of biomass burning in the tropics. *J. Geophys. Res.*, **95**, 9927–9939.

——, A. Gitelson, A. Karnieli, E. Ganor, R. S. Fraser, T. Nakajima, S. Mattoo, and B. N. Holben, 1994: Size distribution and phase function of aerosol particles retrieved from sky brightness measurements. *J. Geophys. Res.*, **99**, 10 341–10 356.

——, D. Tanré, L. A. Remer, E. F. Vermote, A. Chu, and B. N. Holben, 1997a: Operational remote sensing of tropospheric aerosol over land from EOS-Moderate Resolution Imaging Spectroradiometer. *J. Geophys. Res.*, **102**, 17 051–17 067.

——, A. Wald, L. A. Remer, B. C. Gao, R. R. Li, and L. Flynn, 1997b: Remote sensing of aerosol over the continents with the aid of a 2.2 μm channel. *IEEE Trans. Geosci. Remote Sens.*, **36**, 1286–1298.

——, and Coauthors, 1998: The Smoke, Clouds, and Radiation—Brazil (SCAR-B) experiment. *J. Geophys. Res.*, **103**, 31 783–31 808.

Kent, G. S., P. H. Wang, M. P. McCormick, and K. M. Skeens, 1995: Multiyear Stratospheric Aerosol and Gas Experiment-II measurements of upper-tropospheric aerosol characteristics. *J. Geophys. Res.*, **100**, 13 875–13 899.

King, M. D., D. M. Byrne, B. M. Herman, and J. A. Reagan, 1978: Aerosol size distributions obtained by inversion of spectral optical depth measurements. *J. Atmos. Sci.*, **35**, 2153–2167.

——, Y. J. Kaufman, W. P. Menzel, and D. Tanré, 1992: Remote sensing of cloud, aerosol, and water vapor properties from the Moderate Resolution Imaging Spectrometer (MODIS). *IEEE Trans. Geosci. Remote Sens.*, **30**, 2–27.

——, S. C. Tsay, S. A. Ackerman and N. F. Larsen, 1998: Discriminating heavy aerosol, clouds, and fires during SCAR-B: Application of airborne multispectral MAS data. *J. Geophys. Res.*, **103**, 31 989– 32 000.

——, and Coauthors, 1996: Airborne scanning spectrometer for remote sensing of cloud, aerosol, water vapor, and surface properties. *J. Atmos. Oceanic Technol.*, **13**, 777–794.

Koepke, P., 1984: Effective reflectance of oceanic whitecaps. *Appl. Opt.*, **23**, 1816–1824.

——, and H. Quenzel, 1981: Turbidity of the atmosphere determined from satellite: Calculation of optimum wavelength. *J. Geophys. Res.*, **86**, 9801–9805.

Lee, T., and Y. J. Kaufman, 1986: The effect of surface non-Lambertianity on remote sensing of ground reflectance and vegetation index. *IEEE Trans. Geosci. Remote Sens.*, **24**, 699–708.

Legrand, M., M. Desbois, and K. Vovor, 1988: Satellite detection of Saharan dust: Optimized imaging during nighttime. *J. Climate*, **1**, 256–264.

——, J. J. Bertrand, M. Desbois, L. Meneger, and Y. Fouquart, 1989: The potential of infrared satellite data for the retrieval of Saharan dust optical depth over Africa. *J. Appl. Meteor.*, **28**, 309–318.

Leroy, M., and Coauthors, 1997: Retrieval of aerosol properties and surface bidirectional reflectances from POLDER/ADEOS. *J. Geophys. Res.*, **102**, 17 023–17 037.

Long, C. S., and L. L. Stowe, 1994: Using the NOAA/AVHRR to study stratospheric aerosol optical thicknesses following the Mt. Pinatubo eruption. *Geophys. Res. Lett.*, **21**, 2215–2218.

Martins, J. V., Y. J. Kaufman, and P. Artaxo, 1998: Spectral measurements of single scattering albedo from MODIS Airborne Simulator and AVIRIS. *J. Geophys. Res.*, **103**, 32 041–32 050.

Martonchik, J. V., 1997: Determination of aerosol optical depth and land surface directional reflectances using multiangle imagery. *J. Geophys. Res.*, **102**, 17 015–17 022.

——, and D. J. Diner, 1992: Retrieval of aerosol and land surface optical properties from multi-angle satellite imagery. *IEEE Trans. Geosci. Remote Sens.*, **30**, 223–230.

McCormick, M. P., L. W. Thomason, and C. R. Trepte, 1995: Atmospheric effects of the Mt. Pinatubo eruption. *Nature*, **373**, 399–404.

Mekler, Y., H. Quenzel, G. Ohring, and I. Marcus, 1977: Relative atmospheric aerosol content from ERTS observations. *J. Geophys. Res.*, **82**, 967–972.

Mishchenko, M. I., and L. D. Travis, 1997: Satellite retrieval of aerosol properties over the ocean using polarization as well as intensity of reflected sunlight. *J. Geophys. Res.*, **102**, 16 989–17 013.

Moulin, C., F. Guillard, F. Dulac, and C. E. Lambert, 1997: Long-term daily monitoring of Saharan dust load over ocean using Meteosat ISCCP-B2 data, 1, Methodology and preliminary results for 1983–1994 in the Mediterranean. *J. Geophys. Res.*, **102**, 16 947–16 958.

Nadal, F., and F. M. Bréon, 1999: Parameterization of surface polarized reflectance derived from POLDER spaceborne measurements. *IEEE Trans. Geosci. Remote Sens.*, **37**, 1709–1718.

Nakajima, T., and A. Higurashi, 1997: AVHRR remote sensing of aerosol optical properties in the Persian Gulf region, summer 1991. *J. Geophys. Res.*, **102**, 16 935–16 946.

——, and ——, 1998: A use of two-channel radiances for an aerosol characterization from space. *Geophys. Res. Lett.*, **25,** 3815–3818.

——, T. Takamura, M. Yamano, M. Shiobara, T. Yamauchi, R. Goto, and K. Murai, 1986: Consistency of aerosol size distribution inferred from measurements of solar radiation and aureole. *J. Meteor. Soc. Japan*, **64**, 765–776.

Nakajima, T. Y., T. Nakajima, M. Nakajima, H. Fukushima, M. Kuji, A. Uchiyama, and M. Kishino, 1998: Optimization of the Advanced Earth Observing Satellite II Global Imager channels by use of radiative transfer calculations. *Appl. Opt.*, **37**, 3149–3163.

Quenzel, H., and P. Koepke, 1984: Tropospheric aerosol optical depth inverted from upwelling radiances. *Aerosols and Their Climatic Impact*, H. E. Gerber and A. Deepak, Eds., A. Deepak Publ., 227–240.

Rao, C. R. N., L. L. Stowe, and E. P. McClain, 1989: Remote sensing of aerosols over the oceans using AVHRR data: Theory, practice, and applications. *Int. J. Remote Sens.*, **10**, 743–749.

Remer, L. A., and Y. J. Kaufman, 1998: Dynamical aerosol model: Urban/industrial aerosol. *J. Geophys. Res.*, **103**, 13 859–13 871.

——, ——, and B. N. Holben, 1996: The size distribution of ambient aerosol particles: Smoke vs. urban/industrial aerosol. *Global Biomass Burning*, J. S. Levine, Ed., MIT Press, 519–530.

——, ——, ——, A. M. Thompson, and D. McNamara, 1998: A model of tropical biomass burning smoke aerosol size distribution. *J. Geophys. Res.*, **103**, 31 879–31 892.

Russell, P. B., P. V. Hobbs, and L. L. Stowe, 1999a: Aerosol properties and radiative effects in the United States haze plume: An overview of the Tropospheric Aerosol Radiative Forcing Observational Experiment (TARFOX). *J. Geophys. Res.*, **104**, 2213–2222.

——, and Coauthors, 1999b: Aerosol-induced radiative flux changes off the United States mid-Atlantic coast: Comparison of values calculated from sunphotometer and in situ data with those measured by airborne pyranometer. *J. Geophys. Res.*, **104**, 2289–2307.

Schwartz, S. E., and Coauthors, 1995: Group report: Connections between aerosol properties and forcing of climate. *Aerosol Forcing of Climate*, R. J. Charlson and J. Heintzenberg, Eds., John Wiley and Sons, 251–280.

Shenk, W. E., and R. J. Curran, 1974: The detection of dust storms over land and water with satellite visible and infrared measurements. *Mon. Wea. Rev.*, **102**, 830–837.

Soufflet, V., D. Tanré, A. Royer, and N. O'Neil, 1997: Remote sensing of aerosols over boreal forest and lakes from NOAA/AVHRR data. *Remote Sens. Environ.*, **60**, 22–34.

Soulen, P. F., M. D. King, S. C. Tsay, G. T. Arnold, and J. Y. Li, 1999: Airborne spectral measurements of surface-atmosphere anisotropy during the SCAR-A, Kuwait oil fire, and TARFOX experiments. *J. Geophys. Res.*, in press.

Stowe, L. L., R. M. Carey, and P. P. Pellegrino, 1992: Monitoring the Mt. Pinatubo aerosol layer with NOAA/11 AVHRR data. *Geophys. Res. Lett.,* **19**, 159–162.

——, A. M. Ignatov, and R. R. Singh, 1997: Development, validation, and potential enhancements to the second-generation operational aerosol product at the National Environmental Satellite, Data, and Information Service of the National Oceanic and Atmospheric Administration. *J. Geophys. Res.,* **102**, 16 923–16 934.

Takayama, Y., and T. Takashima, 1986: Aerosol optical thickness of yellow sand over the Yellow Sea derived from NOAA satellite data. *Atmos. Environ.,* **20**, 631–638.

Tanré, D., and M. Legrand, 1991: On the satellite retrieval of Saharan dust optical thickness over land: Two different approaches. *J. Geophys. Res.,* **96**, 5221–5227.

——, P. Y. Deschamps, C. Devaux, and M. Herman, 1988: Estimation of Saharan aerosol optical thickness from blurring effects in thematic mapper data. *J. Geophys. Res.,* **93**, 15 955–15 964.

——, E. Vermote, B. N. Holben, and Y. J. Kaufman, 1992: Satellite aerosol retrieval over land surfaces using the structure functions. *Proc. IGARSS'92,* IEEE Geoscience and Remote Sensing Society, Houston, TX, 1474–1477.

——, Y. J. Kaufman, M. Herman, and S. Matoo, 1997: Remote sensing of aerosol properties over oceans using the MODIS/EOS spectral radiances. *J. Geophys. Res.,* **102**, 16 971–16 988.

——, L. A. Remer, Y. J. Kaufman, S. Mattoo, P. V. Hobbs, J. M. Livingston, P. B. Russell, and A. Smirnov, 1999: Retrieval of aerosol optical thickness and size distribution over ocean from the MODIS Airborne Simulator during TARFOX. *J. Geophys. Res.,* **104**, 2261–2278.

Tegen, I., A. A. Lacis, and I. Fung, 1996: The influence on climate forcing of mineral aerosols from disturbed soils. *Nature,* **380**, 419–422.

Torres, O., P. K. Bhartia, J. R. Herman, Z. Ahmad, and J. Gleason, 1998: Derivation of aerosol properties from satellite measurements of backscattered ultraviolet radiation: Theoretical basis. *J. Geophy. Res.,* **103**, 17 099–17 110.

Tsay, S. C., M. D. King, G. T. Arnold, and J. Y. Li, 1998: Airborne spectral measurements of surface anisotropy during SCAR-B. *J. Geophys. Res.,* **103**, 31 943–31 954.

Twomey, S. A., M. Piepgrass, and T. L. Wolfe, 1984: An assessment of the impact of pollution on global cloud albedo. *Tellus,* **36**, 356–366.

Vane, G., R. O. Green, T. G. Chrien, H. T. Enmark, E. G. Hansen, and W. M. Porter, 1993: The Airborne Visible/Infrared Imaging Spectrometer (AVIRIS). *Remote Sens. Environ.,* **44**, 127–143.

Veefkind, J. P., and G. de Leeuw, 1997: A new aerosol retrieval algorithm to determine the spectral aerosol optical depth from satellite radiometer measurements. *J. Aerosol Sci.,* **29**, 1237–1248.

——, ——, and P. A. Durkee, 1998: Retrieval of aerosol optical depth over land using two-angle view radiometry during TARFOX. *Geophys. Res. Lett.,* **25**, 3135–3138.

——, ——, ——, P. B. Russell, P. V. Hobbs, and J. M. Livingston, 1999: Aerosol optical depth retrieval using ATSR-2 and AVHRR data during TARFOX. *J. Geophys. Res.,* **104**, 2253–2260.

Vermote, E., and Y. J. Kaufman, 1995: Absolute calibration of AVHRR visible and near infrared channels using ocean and cloud views. *Int. J. Remote Sens.,* **16**, 2317–2340.

Wang, M., and H. R. Gordon, 1994: Estimating aerosol optical properties over the oceans with MISR: Some preliminary studies. *Appl. Opt.,* **33**, 4042–4057.

Yamasoe, M. A., Y. J. Kaufman, O. Dubovik, L. A. Remer, B. N. Holben, and P. Artaxo, 1998: Retrieval of the real part of the refractive index from sun/sky measurements during SCAR-B. *J. Geophys. Res.,* **103**, 31 893–31 902.